Article

Current Biology

Sensory Neurons Contacting the Cerebrospinal Fluid Require the Reissner Fiber to Detect Spinal Curvature *In Vivo*

Graphical Abstract

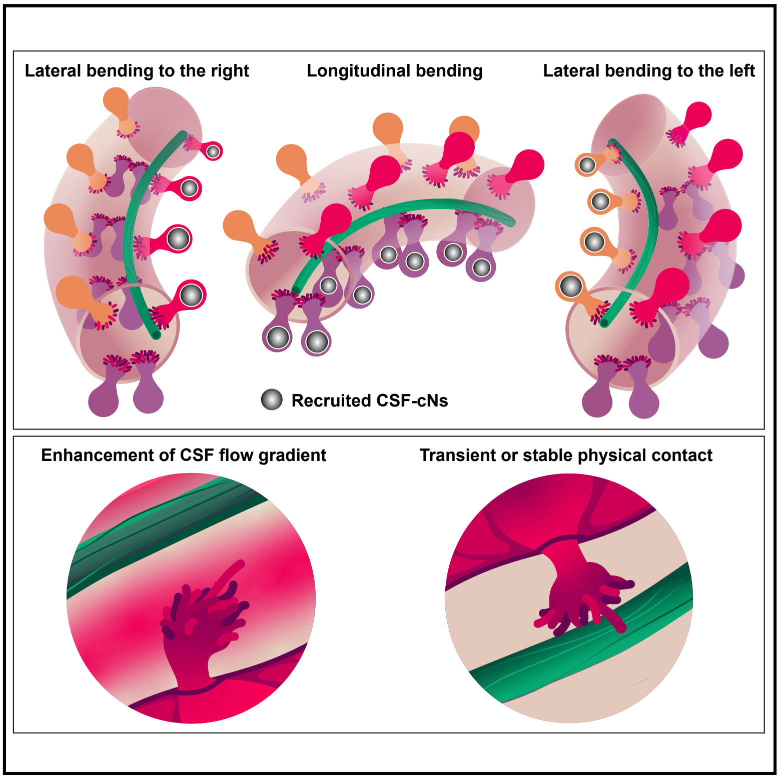

Highlights

- Since its discovery in 1860, the role of the Reissner fiber has been debated
- CSF-contacting neurons (CSF-cNs) are in close vicinity of the Reissner fiber
- Mechanoreception in CSF-cNs requires the Reissner fiber
- CSF-cNs together with the Reissner fiber detect spinal curvature *in vivo*

Authors

Adeline Orts-Del'Immagine,
Yasmine Cantaut-Belarif,
Olivier Thouvenin, ...,
François-Xavier Lejeune,
Pierre-Luc Bardet, Claire Wyart

Correspondence

claire.wyart@icm-institute.org

In Brief

The role of the Reissner fiber, a long extracellular thread running in the cerebrospinal fluid (CSF), has been, since its discovery in 1860, a subject of debate. Orts-Del'Immagine et al. report that the Reissner fiber plays a critical role in the detection of spinal curvature by sensory neurons contacting the CSF.

Orts-Del'Immagine et al., 2020, Current Biology *30*, 1–13
March 9, 2020 © 2019 Elsevier Ltd.
https://doi.org/10.1016/j.cub.2019.12.071

Please cite this article in press as: Orts-Del'Immagine et al., Sensory Neurons Contacting the Cerebrospinal Fluid Require the Reissner Fiber to Detect Spinal Curvature *In Vivo*, Current Biology (2019), https://doi.org/10.1016/j.cub.2019.12.071

Current Biology
Article

CellPress

Sensory Neurons Contacting the Cerebrospinal Fluid Require the Reissner Fiber to Detect Spinal Curvature *In Vivo*

Adeline Orts-Del'Immagine,[1,3] Yasmine Cantaut-Belarif,[1,3] Olivier Thouvenin,[1,2] Julian Roussel,[1] Asha Baskaran,[1] Dominique Langui,[1] Fanny Koëth,[1] Paul Bivas,[1] François-Xavier Lejeune,[1] Pierre-Luc Bardet,[1] and Claire Wyart[1,4,*]
[1]Institut du Cerveau et de la Moelle Épinière (ICM), Sorbonne Université, Inserm U 1127, CNRS UMR 7225, 75013 Paris, France
[2]Institut Langevin ESPCI, PSL Research University, CNRS UMR7587, 1 rue Jussieu, Paris 75005, France
[3]These authors contributed equally
[4]Lead Contact
*Correspondence: claire.wyart@icm-institute.org
https://doi.org/10.1016/j.cub.2019.12.071

SUMMARY

Recent evidence indicates active roles for the cerebrospinal fluid (CSF) on body axis development and morphogenesis of the spine, implying CSF-contacting neurons (CSF-cNs) in the spinal cord. CSF-cNs project a ciliated apical extension into the central canal that is enriched in the channel PKD2L1 and enables the detection of spinal curvature in a directional manner. Dorsolateral CSF-cNs ipsilaterally respond to lateral bending although ventral CSF-cNs respond to longitudinal bending. Historically, the implication of the Reissner fiber (RF), a long extracellular thread in the CSF, to CSF-cN sensory functions has remained a subject of debate. Here, we reveal, using electron microscopy in zebrafish larvae, that the RF is in close vicinity with cilia and microvilli of ventral and dorsolateral CSF-cNs. We investigate *in vivo* the role of cilia and the RF in the mechanosensory functions of CSF-cNs by combining calcium imaging with patch-clamp recordings. We show that disruption of cilia motility affects CSF-cN sensory responses to passive and active curvature of the spinal cord without affecting the Pkd2l1 channel activity. Because ciliary defects alter the formation of the RF, we investigated whether the RF contributes to CSF-cN mechanosensitivity *in vivo*. Using a hypomorphic mutation in the *scospondin* gene that forbids the aggregation of SCO-spondin into a fiber, we demonstrate *in vivo* that the RF per se is critical for CSF-cN mechanosensory function. Our study uncovers that neurons contacting the cerebrospinal fluid functionally interact with the RF to detect spinal curvature in the vertebrate spinal cord.

INTRODUCTION

Cerebrospinal fluid (CSF) is secreted by the choroid plexuses and fills the ventricular cavities of the brain and the central canal of the spinal cord [1]. The CSF has been long assumed to form a passive fluid acting as a cushion, supporting the clearance of toxic products in the brain, thereby ensuring its mechanical protection and chemical homeostasis. However, multiple studies have shown that secretion and circulation of signaling molecules in the CSF contribute in the brain to neurogenesis in an age-dependent manner [2–7]. Furthermore, physicochemical properties of the CSF also contribute to organogenesis outside of the nervous system. CSF content and cilia-driven flow control the geometry of the body axis during embryogenesis [8, 9] as well as spine curvature in juvenile zebrafish [9, 10]. Both the formation of the body axis and the spine organogenesis appear linked to urotensin-related peptides expressed in the spinal cord by cerebrospinal fluid-contacting neurons (CSF-cNs) [9, 11].

CSF-cNs are found in the spinal cord in many vertebrate species [12–14]. Spinal CSF-cNs are GABAergic sensory neurons that extend an apical extension into the lumen of the central canal. This apical extension is composed of one motile cilium and numerous microvilli that bath in the CSF [14–20]. Dorsolateral and ventral CSF-cNs originate from two distinct progenitor domains in zebrafish [18, 19, 21–23] as in mouse [24] and are characterized by different axonal targets [18] and morphology of the apical extension [17]. Both CSF-cN types respond to spinal curvature in a directional manner: although dorsolateral CSF-cNs respond ipsilaterally to lateral bending [16], ventral CSF-cNs are recruited during longitudinal contractions of the spinal cord [25].

Due to the morphological resemblance between CSF-cNs and hair cells, Kolmer had proposed that these cells could constitute a novel sensory organ, referred to as the ‘‘SagittalOrgan,’’ acting as a third ear in the vertebrate spinal cord [13]. This hypothesis has been discussed several times since [12, 26–28], but data were based on sparse electron microscopy and not functional evidence. Identifying genetic markers of CSF-cNs over the last decade [29–31] has allowed novel investigation of their function. Based on these recent studies, we know that spinal CSF-cNs sense changes in pH and osmolarity [32–35] as well as mechanical stretch of the spinal cord [16, 25, 33, 36]. Mechanotransduction in CSF-cNs relies on the polycystic kidney disease 2-like 1 (PKD2L1) channel [16, 36], a member of the transient receptor

Please cite this article in press as: Orts-Del'Immagine et al., Sensory Neurons Contacting the Cerebrospinal Fluid Require the Reissner Fiber to Detect Spinal Curvature *In Vivo*, Current Biology (2019), https://doi.org/10.1016/j.cub.2019.12.071

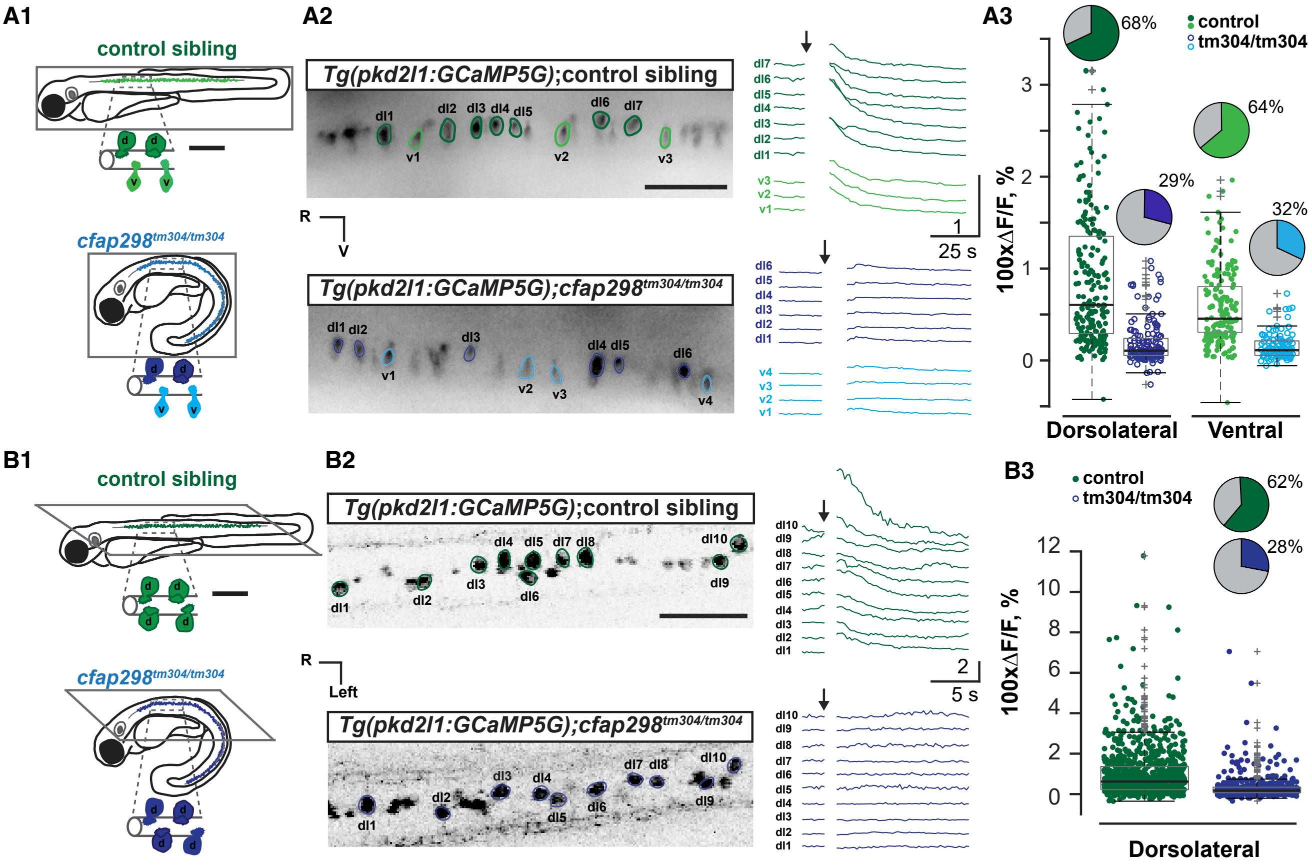

Figure 1. The Sensory Response of CSF-cNs to Spinal Curvature Is Altered in Mutants with Defective Motile Cilia

(A) CSF-cN calcium transients calculated from the changes in fluorescence of the genetically encoded calcium indicator GCaMP5G in 3-dpf *Tg(pkd2l1:GCaMP5G)* transgenic larvae are large for control siblings (top, green) and strongly reduced in *cfap298* $^{tm304/tm304}$ mutants (bottom, blue) during active bends where muscle contraction is induced by pressure application of aCSF in the otic vesicle (see also Videos S1 and S2). (A1) Diagram represents a 3-dpf larva view in sagittal plane. (A2) Time projection stack of 3 optical sections imaged from the sagittal plane (left) shows for illustration purposes a subset of 10 spinal CSF-cNs expressing GCaMP5G in 3-dpf *Tg(pkd2l1:GCaMP5G)*. Green and blue lines around soma delimitate ROIs used to calculate ΔF/F traces on the right. (A3) Quantification of corresponding ΔF/F in dorsolateral and ventral CSF-cNs in control siblings (green) and *cfap298* $^{tm304/tm304}$ mutants (blue) is shown (mean ΔF/F = 87.2% ± 5.0% from 211 dorsolateral CSF-cNs and mean ΔF/F = 57.4% ± 3.3% from 168 ventral cells in 15 control siblings versus mean ΔF/F = 19.0% ± 1.9% from 153 dorsolateral cells and mean ΔF/F = 15.5% ± 1.4% from 104 ventral cells in 11 *cfap298* $^{tm304/tm304}$ larvae, linear mixed model [type II Wald chi-square test]; $p < 1 \times 10^{-4}$ between dorsolateral and ventral CSF-cNs in control siblings, Df = 613; $p < 1 \times 10^{-4}$ between dorsolateral CSF-cNs in mutants versus control siblings, Df = 30.4; $p < 1 \times 10^{-3}$ between ventral CSF-cNs in mutants versus control siblings, Df = 32.9; $p > 0.5$ between dorsolateral and ventral CSF-cNs in *cfap*$^{298tm304/tm304}$ mutants, Df = 614). Pie charts represent the percentage of responding cells (see also Table S1).

(B) CSF-cN calcium transient recorded in 3-dpf *Tg(pkd2l1:GCaMP5G)* transgenic larvae after a passive bend of the tail (passive stimulation) in paralyzed control siblings (top, green) and *cfap298*$^{tm304/tm304}$ mutant fish (bottom, blue). (B1) Diagram shows the coronal plane of a 3 dpf. (B2) Time projection stack of 3 optical sections imaged from the coronal plane (left) shows for illustration purposes a subset of 10 dorsolateral CSF-cNs expressing GCaMP5G in 3-dpf *Tg(pkd2l1:GCaMP5G)*. Green and blue lines around soma delimitate ROIs used to calculate ΔF/F traces upon passive mechanical stimulation represented on the right. (B3) Quantification of corresponding ΔF/F in CSF-cNs represented (as in A2) during a passive bend is shown (mean ΔF/F = 100.7% ± 4.3% from 830 cells in 26 control siblings versus 32.3% ± 2.7% from 490 cells in 15 *cfap298*$^{tm304/tm304}$ larvae, linear mixed model [type II Wald chi-square test]; $p < 2 \times 10^{-9}$; Df = 1; Chi2 = 36.41). Pie charts represent the percentage of responding cells (see also Table S1).

dl, dorsolateral CSF-cNs; R, rostral; V, ventral; v, ventral CSF-cNs. Time projection stacks were constructed from 3 to 4 series of images (corresponding to 0.75–1 s integration time). Each data plotted in (A3) and (B3) represent one recording from one cell, the central mark on the boxplot indicates the median, and the bottom and top edges of the box indicate the 25th and 75th percentiles. The whiskers extend to the most extreme data points that are not considered outliers; outliers are identified with a "+" symbol. Scale bars are 500 μm in (A1) and (B1) and 50 μm in (A2) and (B2) (left panel).

potential (TRP) channel family, which is also a specific marker of these cells in the vertebrate spinal cord [19, 30, 34, 35]. The PKD2L1 channel is enriched in the CSF-cN apical extension [19, 36], which differentiates in the larva and likely constitutes the sensory apparatus of CSF-cNs. Concordantly, the length of microvilli in the apical extension tunes the mechanosensory response of CSF-cNs [17].

In the lumen of the central canal, the Reissner fiber (RF) is a long extracellular thread extending caudally from the diencephalic third ventricle to the central canal of the spinal cord and is mainly composed of the aggregation of the SCO-spondin glycoprotein [26, 37, 38]. A century ago, Kolmer and Agduhr noticed the presence of the RF in close vicinity with the CSF-cN apical extension bathing in the CSF [39]. This proximity

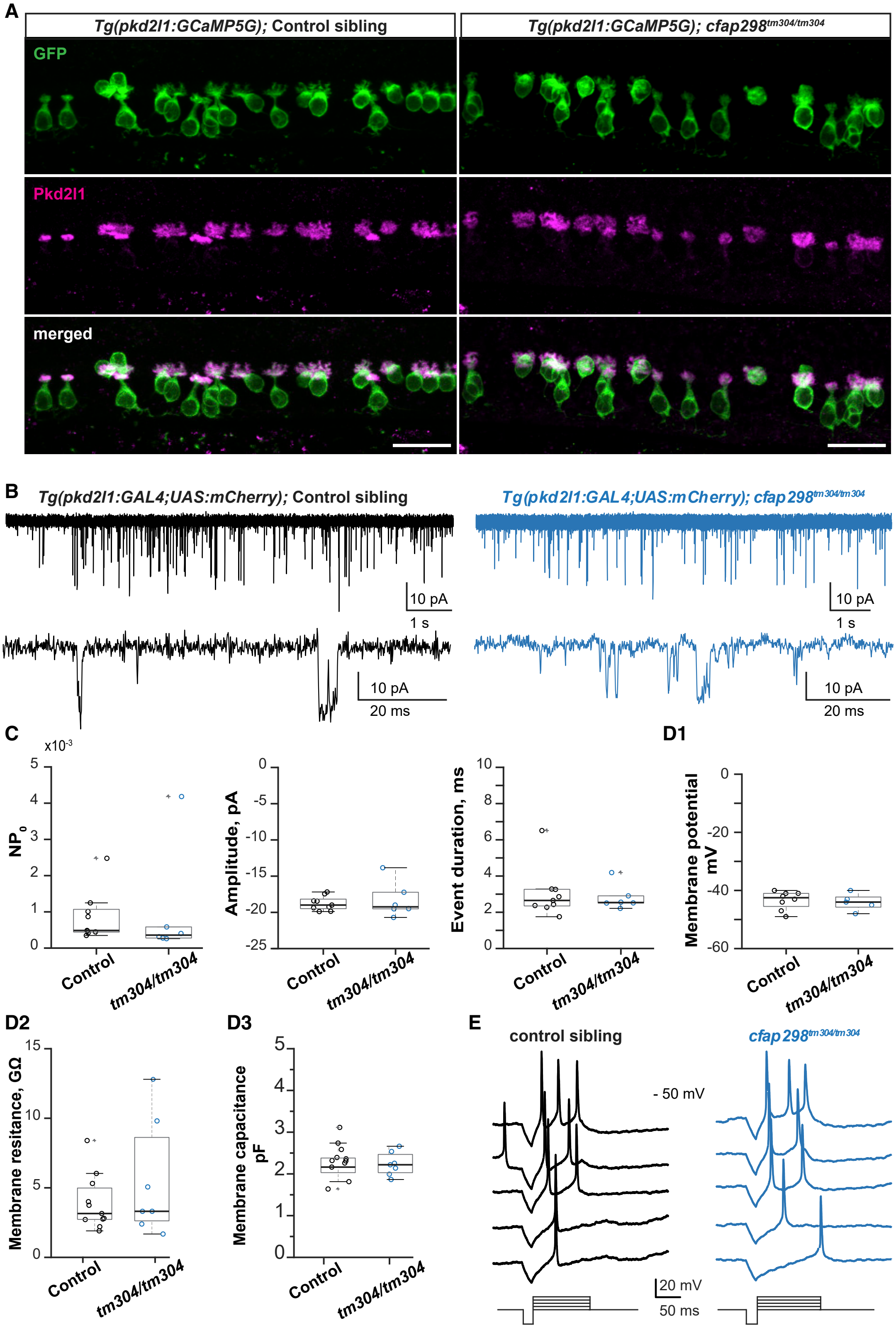

Figure 2. CSF-cNs in *cfap298* Mutant with Defective Motile Cilia Exhibit Functional Pkd2l1 Channels

(A) Immunohistochemistry with anti-GFP and anti-Pkd2l1 antibodies in 3-dpf *Tg(pkd2l1:GCaMP5G)* control sibling (left) and *cfap298*$^{tm304/tm304}$ mutant (right) larvae shows in the spinal cord similar localization for Pkd2l1 protein in the apical extension of CSF-cNs (seen in 14 mutant larvae and 8 control siblings).

(legend continued on next page)

led Kolmer to hypothesize a possible functional interaction between the RF and CSF-cNs [13], a hypothesis not favored by Agduhr [12]. Here, we revisited this question by investigating in zebrafish larvae the role of motile cilia and the RF in CSF-cN mechanotransduction.

We show that disruption of cilia motility affects mechanosensory responses of both ventral and dorsolateral CSF-cNs without affecting Pkd2l1 channel activity. We found using electron microscopy that the RF and CSF-cN apical extension come together in close proximity in the lumen of the central canal. We show that, in *scospondin* hypomorph lacking the fiber in the central canal, CSF-cNs lose their mechanoreception without disrupting Pkd2l1 channel spontaneous opening. Our results demonstrate the need of the RF for transmitting mechanical deformations associated with spinal curvature to sensory neurons lining the central canal. Altogether, our results validate Kolmer's hypothesis, who suggested that CSF-cNs may functionally interact with the RF *in vivo* to form a sensory organ in the vertebrate spinal cord.

RESULTS

Motile Cilia Are Required for CSF-cN Response to Muscle Contraction and Spinal Curvature *In Vivo*

We previously showed that cilia functions are necessary for spontaneous activity of CSF-cNs in the embryos [36]. Now, in order to test the role of motile cilia in CSF-cN response to spinal curvature in the larval stage when their apical extension is differentiated, we induced escape responses in 3 days post-fertilization (dpf) larvae by puffing artificial cerebrospinal fluid (aCSF) in the otic vesicle (Figure 1). We monitored in the sagittal plane CSF-cN activity with the genetically encoded calcium sensor GCaMP5G expressed under the CSF-cN-specific promoter *pkd2l1* in *Tg(pkd2l1:GCaMP5G)* transgenic larvae [18, 29, 36] (Figures 1A1, 1A2, and 1B2; see also Video S1). In this paradigm, larvae were pinned on the side and muscle contractions subsequent to the otic vesicle stimulation occurred in lateral and horizontal directions, which led to calcium transients in dorsolateral and ventral CSF-cNs (Figures 1A2 and 1A3). The amplitude of calcium transient in dorsolateral CSF-cNs was larger than in ventral CSF-cNs (mean $\Delta F/F = 87.2\% \pm 5\%$ from 211 dorsolateral CSF-cNs versus 57.4% ± 3.3% from 168 ventral CSF-cNs in 15 control sibling larvae; linear mixed model [type II Wald chi-square test]: $p < 1 \times 10^{-4}$; see Methods S1), likely due to the muscle contractions being mainly lateral during the escape. We used the $cfap298^{tm304}$ mutation affecting the Cfap298 protein enriched at the base of cilia, which leads to defects in dynein arms, defective motility, and polarity of cilia [40–42]. In the $cfap298^{tm304/tm304}$ mutant larvae, the response of CSF-cNs was overall massively reduced (mean $\Delta F/F = 19.0\% \pm 1.9\%$ from 153 dorsolateral CSF-cNs and 15.5% ± 1.4% from 104 ventral CSF-cNs in 11 mutant larvae; $p < 1 \times 10^{-4}$ for dorsolateral CSF-cNs and $p < 1 \times 10^{-3}$ for ventral CSF-cNs between mutant and control siblings; Figures 1A2 and 1A3; Videos S1 and S2; Table S1). The proportion of CSF-cNs recruited decreased from 68.2% to 29.4% for dorsolateral CSF-cNs and from 64.3% to 31.7% for ventral CSF-cNs (Figure 1A3).

As the *cfap298* mutation may alter cilia in the otic vesicle, defects in inner ear hair cells could be responsible of the decreased response of CSF-cNs. We therefore examined CSF-cN responses to passive curvature of the spinal cord from paralyzed 3 dpf *Tg(pkd2l1:GCaMP5G)* larvae mounted to record from a coronal view dorsolateral CSF-cNs (Figure 1B1) that are selectively activated by lateral bending of the spinal cord [16, 17]. Lateral bending of the tail in control larvae induced, as previously reported [16], calcium transients in dorsolateral CSF-cNs (Figure 1B1). In $cfap298^{tm304/tm304}$ larvae, the response of CSF-cNs was overall massively reduced (mean $\Delta F/F = 32.30\% \pm 2.7\%$ from 490 dorsolateral CSF-cNs in 15 mutant larvae versus 100.7% ± 4.3% from 830 dorsolateral CSF-cNs in 26 control siblings; $p < 2 \times 10^{-9}$; Figures 1B1 and 1B2; Video S2; Table S1; Methods S1). The proportion of dorsolateral CSF-cNs recruited decreased from 62.2% to 28.4% (Figure 1B3). Altogether, our results indicate that cilia motility and polarity are necessary for mechanosensory functions of CSF-cNs *in vivo*.

Mutants with Defective Cilia Maintain Functional Pkd2l1 Channels on CSF-cN Apical Extension

We previously showed that mechanical activation of CSF-cNs requires Pkd2l1 channels *in vivo* [16] and *in vitro* [36]. To confirm the presence and localization of Pkd2l1 at the apical

(B) *In vivo* whole-cell patch-clamp recordings from CSF-cNs using voltage clamp (VC) mode in 3-dpf *Tg(pkd2l1:GAL4;UAS:mCherry)* show single-channel openings in control sibling (left) and in $cfap298^{tm304/tm3040}$ (right). Bottom traces represent at higher temporal magnification the data from top traces.

(C) Data plot of unitary current properties shows that mutant larvae with defective motile cilia show proper spontaneous channel opening properties (mean $NP_0 = 9 \times 10^{-4} \pm 2 \times 10^{-4}$ in control siblings versus $1 \times 10^{-3} \pm 0.6 \times 10^{-3}$ in mutants; two-sample Kolmogorov-Smirnov test, p > 0.5, ks2stat = 0.39; mean unitary current amplitude = −18.8 ± 0.3 pA for control siblings versus −18.3 ± 1.0 pA in mutant larvae, p > 0.8, ks2stat = 0.28; mean duration of single opening = 3.0 ± 0.5 ms in control sibling versus 2.8 ± 0.3 ms in mutant larvae, p > 0.8, ks2stat = 0.28; n = 9 cells in control, n = 6 cells in $cfap298^{tm304/tm304}$ larvae; see also Table S2).

(D) Quantification of CSF-cN basic intrinsic electrophysiological properties (see also Table S3). (D1) CSF-cN resting membrane potential is not affected in $cfap298^{tm304}$ mutant larvae (mean membrane potential = −43.4 ± 1.1 mV in control sibling versus −44.0 ± 1.3 mV in mutant larvae; two-sample Kolmogorov-Smirnov test; p > 0.8; ks2stat = 0.30; n = 8 cells in control; n = 5 cells in $cfap298^{tm304/tm304}$ larvae). (D2) Quantification of membrane resistance reveals no change in $cfap298^{tm304/tm304}$ mutant larvae (mean membrane resistance = 3.9 ± 0.6 GΩ in control siblings versus 5.5 ± 1.6 GΩ in mutant larvae; two-sample Kolmogorov-Smirnov test; p > 0.8; ks2stat = 0.29; n = 11 cells in controls; n = 7 cells in $cfap298^{tm304/tm304}$ larvae). (D3) CSF-cN membrane capacitance is not affected in $cfap298^{tm304}$ mutant larvae (mean membrane capacitance = 2.2 ± 0.1 pF in control sibling versus 2.1 ± 0.1 pF in mutant larvae; two-sample Kolmogorov-Smirnov test; p > 0.2; ks2stat = 0.44; n = 11 cells in control; n = 7 cells in $cfap298^{tm304/tm304}$ larvae).

(E) CSF-cN action potential discharge recorded in current clamp (CC) mode in response to successive current steps (100-ms-long pulses from 2 pA to 10 pA in 2-pA increments).

NP_0, opening probability. Each data point represents one recording from one cell; plots use median as measure of central tendency (central mark on the boxplot), and bottom and top edges of the box indicate the 25th and 75th percentiles. The whiskers extend to the most extreme data points without considering outliers, which are identified with a + symbol. Scale bars are 20 μm in (A).

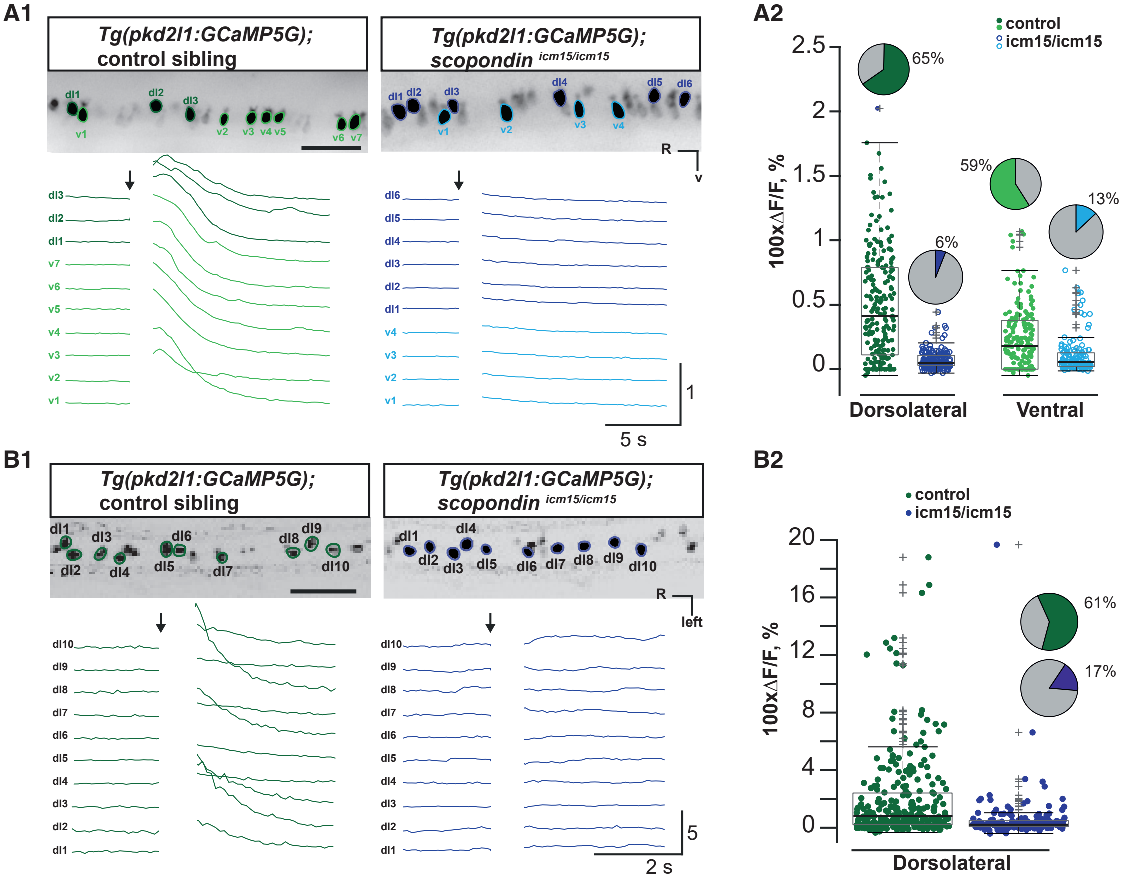

Figure 3. The Absence of the RF Reduces the Sensory Response of CSF-cNs to Spinal Curvature

(A) CSF-cN calcium transient recorded in 3-dpf *Tg(pkd2l1:GCaMP5G)* after active bends due to muscle contraction induced by pressure application of aCSF in the otic vesicle in *scospondin*$^{icm15/icm15}$ mutant larvae (right, blue) and control sibling (left, green; see also Video S3). (A1) Time projection stack of 3 optical sections imaged from the sagittal plane shows dorsolateral and ventral CSF-cNs expressing GCaMP5 (top) in the spinal cord with ROIs on somas (green and blue line) used to calculate ΔF/F traces below. (A2) Quantification of calcium transients in dorsolateral and ventral CSF-cNs in control and *scospondin*$^{icm15/icm15}$ mutants in control sibling (green circle) and mutant larvae (blue circle) is shown (mean ΔF/F = 57.3% ± 3.0% from 180 dorsolateral cells and mean ΔF/F = 31.3% ± 2.1% from 128 ventral cells in 12 control siblings versus mean ΔF/F = 7.1% ± 0.6% from 167 dorsolateral cells and mean ΔF/F = 10.9% ± 1.4% from 146 ventral CSF-cNs in 11 *scospondin*$^{icm15/icm15}$ larvae; linear mixed model [type II Wald chi-square test]; $p < 1 \times 10^{-4}$ between dorsolateral and ventral CSF-cNs in control sibling; Df = 602; $p < 1 \times 10^{-4}$ between dorsolateral CSF-cNs in control siblings versus mutant larvae; Df = 21.4; $p < 5 \times 10^{-4}$ between ventral CSF-cNs in control siblings versus mutant larvae; Df = 22.6; $p > 0.05$ between dorsolateral and ventral CSF-cNs in *scospondin*$^{icm15/icm15}$ larvae; Df = 601). Pie charts represent the percentage of responding cells (see also Table S4).

(B) CSF-cN calcium transient after a passive bend of the tail in paralyzed control siblings (left, green) and *scospondin* $^{icm15/icm15}$ mutant (right, blue) larvae. (B1) Time projection stack of 3 optical sections imaged from the coronal plane shows CSF-cNs expressing GCaMP5 protein (top). ROIs (green and blue lines) used to calculate ΔF/F traces upon passive mechanical stimulation are shown. (B2) Same as (A2) during passive bending is shown (mean ΔF/F = 194.0% ± 17.8% from 276 cells in 11 control siblings versus mean ΔF/F = 56.2% ± 13.1% from 165 cells in 8 *scospondin*$^{icm15/icm15}$ larvae; linear mixed model [type II Wald chi-square test]; $p < 5 \times 10^{-3}$; Df = 1; Chi2 = 8.18; see also Table S4).

Scale bars are 50 μm in (A1) and (B1). Z projection stacks were constructed from 3 series of images (corresponding to 0.75–1 s integration time). For boxplots, each data point in (A2) and (B2) represents one recording from one cell, the central mark indicates the median, and the box bottom and top edges indicate the 25th and 75th percentiles.

extension of CSF-cNs in the *cfap298*$^{tm304/tm304}$ mutant at 3 dpf, we performed immunohistochemistry in *Tg(pkd2l1:GCaMP5G); cfap298*$^{tm304/tm304}$ larvae. Pkd2l1 localized at the apical extension of CSF-cNs in *cfap298*$^{tm304/tm304}$ larvae similarly to control (Figure 2A).

In order to confirm the functionality of Pkd2l1 channels in CSF-cNs, we performed *in vivo* whole-cell voltage clamp recordings in 3 dpf *Tg(pkd2l1:GAL4;UAS:mCherry); cfap298*$^{tm304/tm304}$ larvae. We observed spontaneous Pkd2l1 channel openings with similar properties in both *cfap298*$^{tm304/tm304}$ mutants and their control siblings (Figures 2B and 2C; two-sample Kolmogorov-Smirnov test: $p > 0.5$; Table S2). Furthermore, we did not notice any effect of cilia defects on CSF-cN passive properties (Figures 2D1, 2D2, and 2D3; $p > 0.2$; Table S3) or firing patterns upon current injection (Figure 2E). Hence, cilia impairment decreases CSF-cN mechanosensory function without affecting their intrinsic excitability or Pkd2l1 spontaneous channel openings.

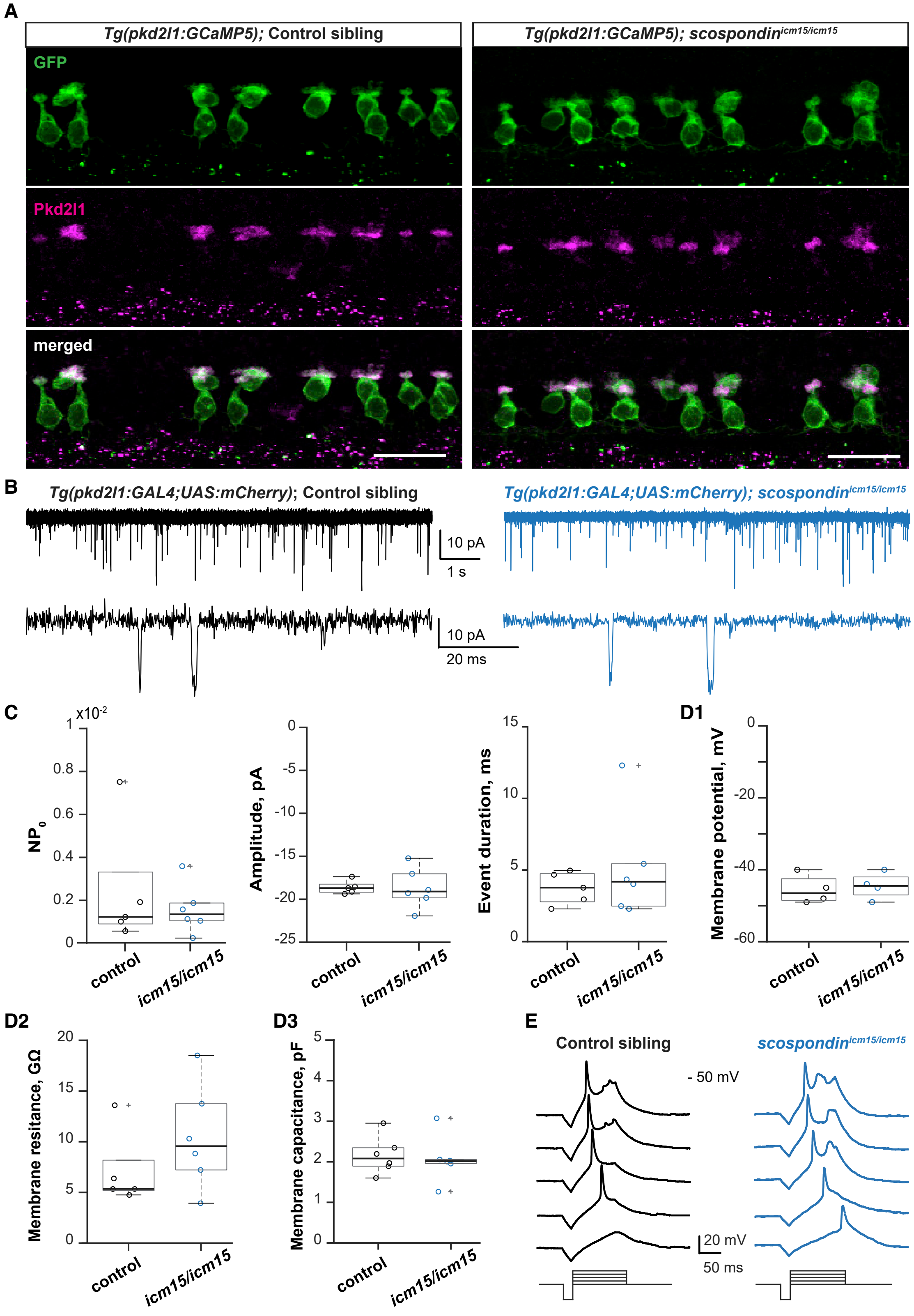

Figure 4. *scospondin* Mutants Deprived of the RF Exhibit Functional Pkd2l1 Channels

(A) Immunohistochemistry for GFP and Pkd2l1 in 3-dpf *Tg(pkd2l1:GCaMP5G)* control siblings (left) and *scospondin*$^{icm15/icm15}$ mutant larvae (right) shows that Pkd2l1 protein is localized in CSF-cN apical extension (sagittal view; n = 15 control sibling and 9 mutant larvae).

(legend continued on next page)

Please cite this article in press as: Orts-Del'Immagine et al., Sensory Neurons Contacting the Cerebrospinal Fluid Require the Reissner Fiber to Detect Spinal Curvature *In Vivo*, Current Biology (2019), https://doi.org/10.1016/j.cub.2019.12.071

Mechanosensory Function of CSF-cNs Requires the RF

The *cfap298*^{tm304} mutation affecting cilia polarity and motility [40, 42] has been shown to (1) reduce CSF flow [10, 43] and CSF transport [36], (2) reduce the diameter of the central canal [43], and (3) forbid the formation of the RF [8]. Parameters such as CSF flow, diameter of the central canal, and the presence of the RF could all contribute to the defect observed in CSF-cN sensory function.

Because the role of the RF in spinal mechanoreception is of peculiar interest, we took advantage of the hypomorphic mutation *scospondin*^{icm15} in the gene *scospondin*, in which a 5-amino-acid insertion in the Emilin domain forbids the aggregation of SCO-spondin into the RF [8]. Response of dorsolateral and ventral CSF-cN to active tail bending was largely abolished in *Tg(pkd2l1:GCaMP5G); scospondin*$^{icm15/icm15}$ mutant larvae (Figures 3A1 and 3A2; Video S3; Table S4; dorsolateral CSF-cNs: mean $\Delta F/F = 57.3\% \pm 3.0\%$ from 180 cells in 12 control sibling versus $7.1\% \pm 0.6\%$ from 167 cells in 11 mutant larvae; linear mixed model [type II Wald chi-square test]: $p < 1 \times 10^{-4}$; ventral CSF-cNs: mean $\Delta F/F = 31.3\% \pm 2.1\%$ from 128 cells in control sibling versus $10.9\% \pm 1.4\%$ from 146 cells from mutant larvae; linear mixed model [type II Wald chi-square test]: $p < 5 \times 10^{-4}$; see Methods S1). In response to passive tail bending (Figure 3B1), the calcium transients recorded in dorsolateral CSF-cNs showed a 3-fold reduction in *scospondin*$^{icm15/icm15}$ mutant larvae (Figure 3B2; mean $\Delta F/F = 194.0\% \pm 17.8\%$ from 276 cells in 11 control siblings versus $56.2\% \pm 13.1\%$ from 165 cells from in mutant larvae; $p < 0.005$; see Methods S1). In the active assay, the proportion of dorsolateral CSF-cNs recruited was decreased by 90.8% and by 77.8% for ventral CSF-cNs (Figure 3A2). After passive stimulation, the proportion of responding dorsolateral CSF-cNs was decreased by 72.1% (Figure 3B2; Table S4). Altogether, our results demonstrate that CSF-cNs require the RF to optimally respond to mechanical stimuli associated with spinal curvature *in vivo*.

Pkd2l1 Channels in CSF-cNs Remain Functional when the RF Is Absent

The RF could be required for CSF-cNs to express the Pkd2l1 channel at the membrane. To verify that CSF-cNs properly express Pkd2l1 in their apical extension, we first performed immunohistochemistry on *Tg(pkd2l1:GCaMP5G); scospondin*$^{icm15/icm15}$ and found that the Pkd2l1 protein was still enriched in CSF-cN apical extension of larvae lacking the RF (Figure 4A). Accordingly, whole-cell patch-clamp recording of CSF-cNs in *Tg(pkd2l1:GAL4;UAS:mCherry); scospondin*$^{icm15/icm15}$ revealed spontaneous unitary current (Figures 4B and 4C; two-sample Kolmogorov-Smirnov test: $p > 0.8$; Table S5), most likely reflecting functional Pkd2l1 channels [34, 36]. We tested whether the absence of the RF could affect the intrinsic properties of CSF-cNs and found no difference in membrane resistance, membrane capacitance, or resting membrane potential (Figures 4D1–4D3; $p > 0.07$; Table S6). The firing pattern of CSF-cNs in *scospondin*$^{icm15/icm15}$ upon current injection was comparable to controls (Figure 4E). Altogether, our results show that the absence of the RF does not alter the localization of Pkd2l1 channel to the apical extension, the spontaneous Pkd2l1 channel properties, or the intrinsic excitability of CSF-cNs.

In the Central Canal, the RF Is in Close Vicinity with CSF-cN Apical Extension

Given that, in the absence of the RF, CSF-cN sensitivity to spinal curvature is largely reduced despite the cells retaining their intrinsic properties and Pkd2l1 channel activity, we investigated where the RF is localized in the central canal relative to the apical extension of CSF-cNs. In live larvae, the lumen of the central canal is typically 8.7 ± 0.4 μm width and 10.2 ± 0.7 μm height (measured from 4 and 9 larvae, respectively; Figures 5A, 5C, and 5D; Table S7) and CSF-cNs extend their dendritic apical extension by typically 2.9 ± 0.1 μm height (measured from 9 cells in 4 larvae; Table S7) toward the center of the central canal, suggesting that CSF-cNs cover a substantial portion of the central canal in living zebrafish larvae.

To assess the relative organization of the RF and CSF-cN apical extension, we immunostained for the RF material as previously described [8] in 3 dpf *Tg(pkd2l1:GAL4;UAS:tagRFP-CAAX)* larvae. As the process of fixation can alter the shape of cavities filled with CSF, such as the central canal, we determined the impact of fixation on the width and height of the central canal measured in 3 dpf *Tg(cdh2:cdh2-GFP; pkd2l1:GAL4;UAS:tagRFP)* larvae imaged live and after fixation followed by either

(B) *In vivo* whole-cell patch-clamp recording of CSF-cNs in voltage clamp (VC) mode targeted for mCherry in 3-dpf *Tg(pkd2l1:GAL4;UAS:mCherry)* exhibits single channel opening in control sibling (left) and in *scospondin*$^{icm15/icm15}$ mutant (right) larva. Bottom traces represent a higher magnification from the top trace.

(C) Unitary currents reflecting spontaneous channel opening properties are not affected in *scospondin*$^{icm15/icm15}$ mutants compared to control siblings (mean $NP_0 = 2.4 \times 10^{-3} \pm 1.3 \times 10^{-3}$ in control sibling versus $1.6 \times 10^{-3} \pm 0.5 \times 10^{-3}$ in mutant; two-sample Kolmogorov-Smirnov test, $p > 0.9$, ks2stat = 0.23; mean unitary current amplitude = -18.6 ± 0.3 pA in control sibling versus -18.7 ± 0.9 pA in mutant larvae, $p > 0.8$, ks2stat = 0.33; mean duration of single opening = 3.7 ± 0.5 ms in control sibling versus 5.1 ± 1.5 ms in mutant larvae, $p > 0.8$, ks2stat = 0.33; n = 5 cells in control siblings; n = 6 cells in *scospondin*$^{icm15/icm15}$ larvae; see also Table S5).

(D) Quantification of CSF-cN basic intrinsic electrophysiological properties (see also Table S6). (D1) CSF-cN resting membrane potential remains unaffected in *scospondin*$^{icm15/icm15}$ mutants (mean membrane potential = -45.5 ± 2.0 mV, n = 4 cells in control sibling versus -44.5 ± 1.8 mV, n = 4 cells in mutant larvae; two-sample Kolmogorov-Smirnov test; $p > 0.9$; ks2stat = 0.25). (D2) CSF-cN membrane resistance is not altered in *scospondin*$^{icm15/icm15}$ mutants (mean membrane resistance = 6.9 ± 1.4 GΩ in control sibling versus 10.4 ± 2.1 GΩ in mutant larvae; two-sample Kolmogorov-Smirnov test; $p > 0.08$; ks2stat = 0.67; n = 6 cells in control; n = 6 cells in *scospondin*$^{icm15/icm15}$ larvae). (D3) CSF-cN membrane capacitance is comparable between *scospondin*$^{icm15/icm15}$ mutants and control larvae (mean membrane capacitance = 2.2 ± 0.2 pF, n = 6 cells in control sibling versus 2.1 ± 0.2 pF, n = 6 cells in *scospondin*$^{icm15/icm15}$ larvae; two-sample Kolmogorov-Smirnov test; $p > 0.8$; ks2stat = 0.33).

(E) Discharge of action potential in CSF-cNs recorded in CC mode in response to successive current steps (100-ms-long pulses from 2 pA to 10 pA in 2-pA increments).

Scale bars are 20 μm in (A). Each data point represents one recording from one cell; plots use median as measure of central tendency (central mark on the boxplot), and the bottom and top edges of the box indicate the 25th and 75th percentiles. The whiskers extend to the most extreme data points without considering outliers, and the outlier is identified with a + symbol.

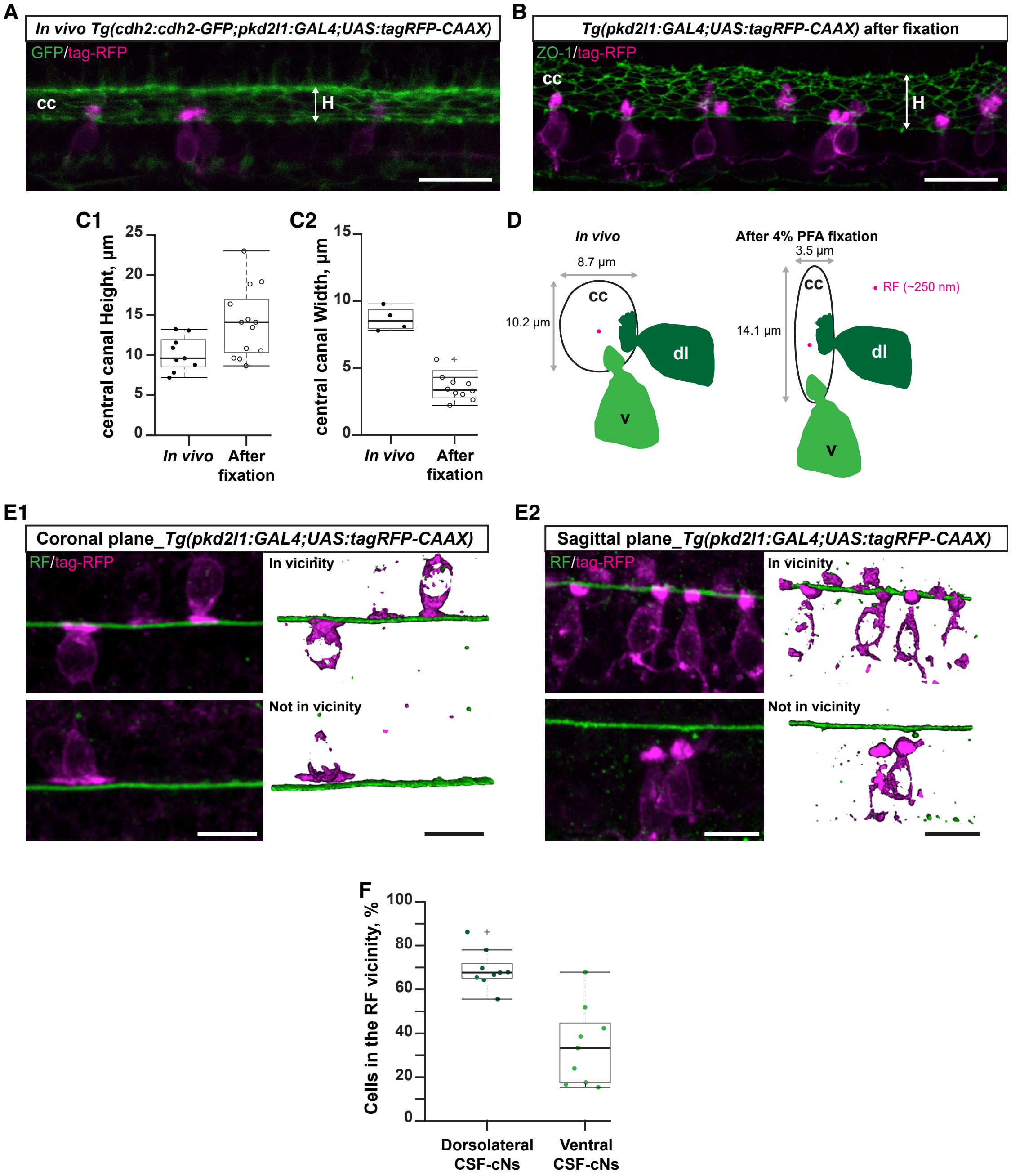

Figure 5. The RF Is in Close Vicinity of the Apical Extension of CSF-cNs

(A) Z projection stack of a few optical sections imaged in the sagittal plane in living 3-dpf *Tg(cdh2:cdh2-GFP; pkd2l1:GAL4;UAS:tagRFP-CAAX)* larvae shows the height of the central canal *in vivo*.

(B) Z projection stack of a few optical sections imaged in the sagittal plane in 3-dpf *Tg(pkd2l1:GAL4;UAS:tagRFP-CAAX)* larvae after co-immunostaining for ZO-1 and tag-RFP used to measure the height of the central canal in fixed whole-mount larva.

(C) Comparison of the size of the central canal between live and fixed whole-mount 3-dpf larva reveals an artifact of fixation (see also Table S7). (C1) Measurement of the height of the central canal shows that the central canal has a higher height after fixation (mean height = 10.2 ± 0.7 μm from 9 live larvae versus 14.1 ± 1.2 μm in 13 fixed whole-mount larvae; two-sample Kolmogorov-Smirnov test; $p < 0.03$; ks2stat = 0.62). (C2) Measurement of the width of the central canal reveals that the central canal is two times narrower after fixation (mean width = 8.7 ± 0.4 μm from 4 live larvae versus 3.5 ± 0.3 μm in 10 fixed whole-mount larvae; two-sample Kolmogorov-Smirnov test; $p < 2 \times 10^{-3}$; ks2stat = 1).

(D) Diagram representing the effect of 4% PFA fixation on the shape of the central canal.

(E) Z projection stack of a few optical sections imaged after immunohistochemistry for tag-RFP and Reissner material in 3-dpf *Tg(pkd2l1:GAL4;UAS:tagRFP-CAAX)* larvae reveals that the apical extension of dorsolateral and ventral CSF-cNs are in close vicinity of the RF. (E1) Dorsolateral CSF-cNs observed in coronal

(legend continued on next page)

co-immunostaining for GFP and tag-RFP or ZO-1 and tag-RFP (Figures 5A–5D). Paraformaldehyde (PFA) fixation induced a shrinking of the central canal along the midline (Figures 5A and 5B): in the transverse plane, the lumen of the central canal after fixation became narrower (3.5 ± 0.3 μm; two-sample Kolmogorov-Smirnov test: $p < 0.05$) and more elongated along the dorsoventral axis (14.1 ± 1.2 μm; $p < 0.002$; Figures 5C and 5D; Table S7). In these conditions, we investigated the approximate position of the RF relative to the apical extension of dorsolateral (Figure 5E1) and ventral (Figure 5E2) CSF-cNs in 3 dpf *Tg(pkd2l1:GAL4;UAS:tagRFP-CAAX)* larvae co-immunostained for RF and tag-RFP. The RF was in close vicinity of two-thirds of dorsolateral CSF-cNs (Figures 5E1, top panel, and 5F) and one-third of ventral CSF-cNs (Figures 5E2, top panel, and 5F; two-sample Kolmogorov-Smirnov test: $p < 5 \times 10^{-4}$).

At higher resolution, we characterized the ultrastructure of the central canal in sagittal sections of 3 to 4 dpf wild-type larvae using transmission electron microscopy (Figure 6). In single sections (Figures 6A and 6B) and reconstruction of the RF and cilia in 3D using serial block face scanning electron microscope imaging (Figures 6C and 6D), the RF appeared as a long and thin thread (Figures 6A and 5B) with diameter of 258.4 ± 6.8 nm (26 measurements from 2 larvae) often in close contact with cilia (arrows) and microvilli (arrowheads; Figure 6A). Cilia in contact with the RF had two central microtubules along the axoneme (Figures 6A1, 6A2, 6A3, and 6A4), which typically characterize motile cilia found in ependymal radial glia [36, 44–46] as well as CSF-cNs [16]. CSF-cNs have one motile cilium and many microvilli [16–18]. In these ultrastructure images, a subset of dorsolateral and ventral CSF-cNs extended toward the RF via both their microvilli (Figures 6A1 and 6B, arrowheads) and their motile cilium (Figures 6B–6D; see also Video S4).

DISCUSSION

Our study demonstrates *in vivo* the functional coupling between the RF and neurons contacting the cerebrospinal fluid in the spinal cord in order to detect spinal curvature. By analyzing the physiological and sensory properties of CSF-cNs in the *scospondin*^{icm15} mutant lacking the RF, we proved that Kolmer was correct when he speculated that neurons contacting the cerebrospinal fluid form a mechanosensory organ with the RF in the vertebrate spinal cord [13].

The RF Functionally Interacts with CSF-cNs to Sense Spinal Curvature *In Vivo*

We had formerly showed that CSF-cNs integrate *in vivo* mechanosensory inputs on the concave side during spinal curvature [16, 17] in order to respond to lateral bending for dorsolateral CSF-cNs [16, 17] and longitudinal bending for ventral CSF-cNs [25]. *In vivo*, this directional mechanosensory response of CSF-cNs requires the channel Pkd2l1 [16]. Recently, we showed that CSF-cNs, when isolated *in vitro*, keep their mechanosensory properties: the open probability of the channel Pkd2l1 is largely modulated by mechanical pressure on CSF-cN membrane [36]. Now, we made a new step in understanding how CSF-cNs detect curvature *in vivo*: we demonstrate that the RF enhance by at least 3-fold the response of CSF-cNs to spinal curvature *in vivo*.

Note that, in *cfap298* mutants, the disruption of cilia motility leads to the absence of the RF [8], together with a reduction in the dimensions of the central canal lumen [43]. In these mutants, we cannot exclude that the narrow central canal lumen could also contribute with the loss of RF to the reduction of CSF-cN response. However, as RF loss is the only defect observed in the *scospondin*^{icm15} mutant (the dimensions of the current clamp [CC] and cilia motility are not altered in this mutant), we formulate the parsimonious assumption that the RF is the important factor in explaining the loss of CSF-cN mechanosensory response.

How Can the RF and CSF-cNs Interact to Sense Spinal Curvature?

Recent evidence based on the labeling of SCO-spondin-GFP have revealed that the RF *in vivo* is dynamic as well as straight as an arrow [47], which indicates that the fiber is under high tension *in vivo*. Given the dimensions of the central canal in living larvae (typically 10 μm by 9 μm) compared to the height of CSF-cN apical extensions (typically 3–5 μm) and the very thin diameter of the fiber (~200 nm), it is conceivable that, at rest, the thin RF could sit in the center of the central canal away from CSF-cN apical extension. In contrast, when muscles contract on one side—left, right, or ventrally—the RF under tension could get closer to CSF-cNs during bending, which would enable their selective asymmetrical recruitment in the concave side [16, 17].

The nature of the functional interaction between the RF and CSF-cN apical extension could rely on a transient or stable physical contact, which would amplify the mechanical force applied on the apical extension of CSF-cNs in an asymmetrical manner on the concave side during bending. Alternatively, from the fluid dynamics point of view, it is also highly conceivable that RF and CSF-cN apical extension *functionally* interact without the need for *physical* contacts. Indeed, the RF could increase the CSF flow gradient perceived by CSF-cN apical extension. We previously showed that CSF flow in the central canal is maximal close to the center and null along the central canal walls [43]. Remarkably, the most commonly used boundary condition in fluid dynamics is the non-slip condition, which claims that the velocity of the fluid at a solid wall is the same as that of the solid wall [48]. Therefore, CSF flow has to equalize the velocity of the fiber on the surface of the fiber itself (around 50–200 nm/s at most)

plane are found in the vicinity of the RF (top panel, in vicinity) or further away (bottom panel, not in vicinity). Panel on the right represents a 3D reconstruction from the Z stack on the left. (E2) Same as (E1) imaged in the sagittal plane in order to visualize the proximity of ventral CSF-cNs with the RF.

(F) Dorsolateral CSF-cNs imaged in the coronal plane more often appear in close proximity to the RF than ventral CSF-cNs imaged in sagittal plane (mean fraction in vicinity = 69.0% ± 2.9% from 281 dorsolateral CSF-cNs in 9 larvae versus 34.2% ± 6.0% from 213 ventral CSF-cNs in 9 larvae; two-sample Kolmogorov-Smirnov test; $p < 5 \times 10^{-4}$; ks2stat = 0.89).

Scale bars are 20 μm in (A) and (B) and 10 μm in (E1) and (E2). cc: central canal; H, height; RF, the Reissner fiber. Each data point represents one measure from one fish; plots use median as measure of central tendency (central mark on the boxplot), and the bottom and top edges of the box indicate the 25th and 75th percentiles. The whiskers extend to the most extreme data points without considering outliers, and the outlier is identified with a + symbol.

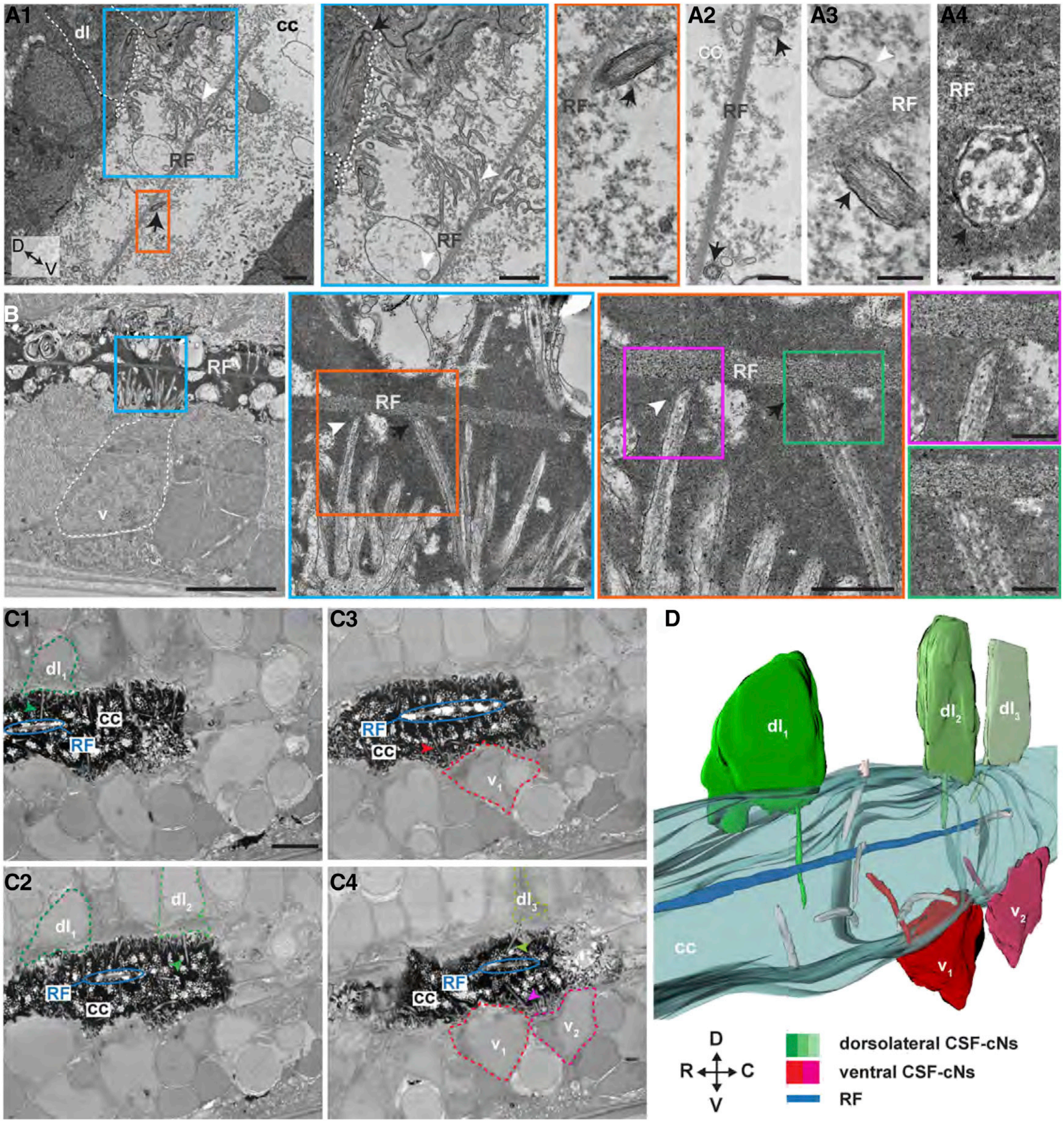

Figure 6. The RF Can Contact Cilia and Microvilli of CSF-cNs in the Central Canal

(A and B) Transmission electron microscopy (TEM) from spinal cord sectioned in the sagittal plane reveals motile cilium (black arrow) near or in contact with the RF as well as microvilli from CSF-cNs (white arrowhead) near RF. Zoomed regions highlighted in different colors. (A1) The RF tends to be dorsally located in the central canal and close to cilia (arrow), as well as microvilli (arrowhead) originating from identifiable dorsolateral CSF-cNs. (A2–A4) Appositions onto the RF of motile cilia, which contain two central microtubules along the axoneme (arrow in A2 and A4), as well as microvilli from a ventral CSF-cN (arrowhead, A3).

(B) Zooms of lateral regions delineated in colored lines show that ventral CSF-cNs can apparently contact the RF via their microvilli (arrowheads) and their motile cilium (arrows).

(C) Z projection stack of 3 subsequent images acquired in the sagittal plane from serial block face scanning electron microscopy (SBF-SEM), highlighting apparent contacts between RF (blue ellipse) and dorsolateral CSF-cNs. (C1)–(C4) correspond to different positions in the sagittal plane where multiple dorsolateral and ventral CSF-cNs can be observed along the rostro-caudal axis (see Video S4).

(D) 3D reconstruction after SBF-SEM imaging (60 sections of 40-nm Z steps and 7-nm thickness) shown in (C) and in Video S4.

Scale bars are 1 μm in (A1) and (A2), 200 nm in (A3) and (A4), 2 μm in (B), 1 μm in blue line delineated in (B), 500 nm in orange line delineated in (B), 200 nm in pink and green lines delineated in (B), and 5 μm in (C). C, caudal. Note that the background signal in the central canal obtained by TEM varies depending on the fixation methods: light background signal for PFA/trichloroacetic acid (TCA) in (A1)–(A3) and dense background signal for PFA/glutaraldehyde in (A4), (B), and (C).

[47], which is negligible compared to the velocity of particles in the flow (around 10 μm/s) [43]. Therefore, CSF-cN apical extension pointing toward the center of the lumen sits in a region of high CSF flow gradient precisely at the boundary between the high flow and the close-to-null flow point imposed by the RF. This effect could be amplified by that CSF flow is largely increased by muscle contractions along the tail as reported in the brain ventricles [49] and in the central canal [43].

Due to the fixation artifact that we quantified here with classical immunostaining protocol, further investigations of the dynamic interactions of CSF-cN apical extensions together with labeled RF *in vivo* [47] occurring during spinal curvature will be necessary to distinguish between these hypotheses.

Comparison of CSF-cNs with Inner Ear Hair Cells

Kolmer and Agduhr originally compared CSF-cNs to hair cells due to the morphological similarity of the apical extension of both cell types. A century later, can we comment on the similarity of mechanisms underlying their mechanosensory functions? Of course, CSF-cNs with their coral-like-shaped microvilli lack the regular staircase organization of stereocilia. However, CSF-cNs bear a kinocilium [15, 16, 50], similarly to inner ear hair cells from fish and amphibians [51]. We know from hair cells in amphibians that the active oscillations of the hair bundle amplify mechanical stimuli, which contributes to sound detection [52]. Similarly to vertebrate hair cells, mechanosensory transduction in the chordotonal sensory neurons that mediate hearing in *Drosophila* rely on the axonemal dynein of motile cilia [53, 54]. Similarly, through active movements, CSF-cN kinocilium could contribute to the amplification of mechanosensory response. The specific role of CSF-cN kinocilium in mechanoreception will be the focus of future investigations based on tools for disrupting cilia only in CSF-cNs and not in other cell types.

Relevance for Development of Body Axis and Spine

Sensory systems are critical to guide symmetrical growth and balanced activation of motor circuits, but they can be also relevant for morphogenesis. We previously showed that CSF-cNs modulate the spinal circuits controlling locomotion and active posture [16, 25, 29, 31, 36]. Recently, the RF and CSF-cNs have also been associated with the establishment of the body axis during embryogenesis [8] and of the spine morphogenesis in juvenile and adult zebrafish [9, 36]. Multiple evidence suggests that CSF-cNs are relevant for spine morphogenesis: *pkd2l1* mutants deprived of CSF-cN sensory responses exhibit an increased curvature of the spine, reminiscent of kyphosis [36]. Furthermore, mutants for a receptor of the urotensin-related peptides, which are solely produced by CSF-cNs in the spinal cord, exhibit a torsion of the spine, reminiscent of adolescent idiopathic scoliosis [9]. Finally, a recent report indicated that hypomorphic mutations in the *scospondin* gene induce 3D deformation of the spine [47]. Altogether, recent studies indicate that sensory neurons contacting the cerebrospinal fluid together with the RF may contribute to the generation and maintenance of the shape of the spine. Future studies will investigate whether the functional coupling of CSF-cNs with the RF that we have demonstrated here is relevant for sensing and adjusting morphogenesis of the spine.

STAR★METHODS

Detailed methods are provided in the online version of this paper and include the following:

- KEY RESOURCES TABLE
- LEAD CONTACT AND MATERIALS AVAILABILITY
- EXPERIMENTAL MODEL AND SUBJECT DETAILS
- METHOD DETAILS
  - ○ Immunohistochemistry
  - ○ Analysis of the proximity between CSF-cNs and the RF
  - ○ Morphological Analysis
  - ○ Calcium imaging
  - ○ *In vivo* patch-clamp recording
  - ○ Electron microscopy
- QUANTIFICATION AND STATISTICAL ANALYSIS
  - ○ Patch-clamp recording and Morphological study
  - ○ Calcium imaging
- DATA AND CODE AVAILABILITY

SUPPLEMENTAL INFORMATION

Supplemental Information can be found online at https://doi.org/10.1016/j.cub.2019.12.071.

ACKNOWLEDGMENTS

We thank Monica Dicu and Antoine Arneau for fish care. We thank Céline Revenu for sharing the *Tg(cdh2:cdh2-GFP,crybb1:ECFP)* transgenic line, Remi Leborgne from the ImagoSeine facility (Jacques Monod Institute Paris, France), and the France BioImaging infrastructure supported by the French National Research Agency (ANR-10-INSB-04, « Investments fit the future ») for precious help in serial block face scanning electron microscope imaging. We thank for critical feedback all members of the Wyart lab (https://wyartlab.org/). Part of this work was carried out in the Phenoparc and ICM.Quant core facilities of ICM. This work was supported by an ERC Starting Grant "Optoloco" no. 311673 and New York Stem Cell Foundation (NYSCF) Robertson Award 2016 grant no. NYSCF-R-NI39, the Human Frontier Science Program (HFSP) Program Grants nos. RGP0063/2014 and RGP0063/2018, and the Fondation Schlumberger pour l'Education et la Recherche (FSER/2017) for C.W. The research leading to these results has received funding from the program "Investissements d'avenir" ANR-10-IAIHU-06 (Big Brain Theory ICM Program) and ANR-11-INBS-0011—NeurATRIS: Translational Research Infrastructure for Biotherapies in Neurosciences.

AUTHOR CONTRIBUTIONS

A.O.-D. performed all calcium imaging and electrophysiology experiments and analysis, A.O.-D. and Y.C.-B. performed immunohistochemistry and confocal microscopy imaging, A.B. and D.L. performed electron microscopy (EM), O.T. provided guidance on automated analysis for calcium imaging, J.R. and F.K. helped with genotyping, P.B. provided help for 3D reconstruction, F.-X.L. performed statistical analysis, P.-L.B. provided feedback on morphological analysis, and C.W. conceived, funded, and supervised the project. A.O.-D. and C.W. conceived the project and wrote the article with input from Y.C.-B., P.-L.B., and all authors.

DECLARATION OF INTERESTS

The authors declare no competing interests.

Received: August 20, 2019
Revised: November 28, 2019
Accepted: December 24, 2019
Published: February 20, 2020

REFERENCES

1. Lun, M.P., Monuki, E.S., and Lehtinen, M.K. (2015). Development and functions of the choroid plexus-cerebrospinal fluid system. Nat. Rev. Neurosci. *16*, 445–457.
2. Codega, P., Silva-Vargas, V., Paul, A., Maldonado-Soto, A.R., Deleo, A.M., Pastrana, E., and Doetsch, F. (2014). Prospective identification

Please cite this article in press as: Orts-Del'Immagine et al., Sensory Neurons Contacting the Cerebrospinal Fluid Require the Reissner Fiber to Detect Spinal Curvature *In Vivo*, Current Biology (2019), https://doi.org/10.1016/j.cub.2019.12.071

and purification of quiescent adult neural stem cells from their in vivo niche. Neuron *82*, 545–559.

3. Doetsch, F., Petreanu, L., Caille, I., Garcia-Verdugo, J.M., and Alvarez-Buylla, A. (2002). EGF converts transit-amplifying neurogenic precursors in the adult brain into multipotent stem cells. Neuron *36*, 1021–1034.
4. Lehtinen, M.K., Zappaterra, M.W., Chen, X., Yang, Y.J., Hill, A.D., Lun, M., Maynard, T., Gonzalez, D., Kim, S., Ye, P., et al. (2011). The cerebrospinal fluid provides a proliferative niche for neural progenitor cells. Neuron *69*, 893–905.
5. Paul, A., Chaker, Z., and Doetsch, F. (2017). Hypothalamic regulation of regionally distinct adult neural stem cells and neurogenesis. Science *356*, 1383–1386.
6. Silva-Vargas, V., Maldonado-Soto, A.R., Mizrak, D., Codega, P., and Doetsch, F. (2016). Age-dependent niche signals from the choroid plexus regulate adult neural stem cells. Cell Stem Cell *19*, 643–652.
7. Silva-Vargas, V., and Doetsch, F. (2014). A new twist for neurotrophins: endothelial-derived NT-3 mediates adult neural stem cell quiescence. Neuron *83*, 507–509.
8. Cantaut-Belarif, Y., Sternberg, J.R., Thouvenin, O., Wyart, C., and Bardet, P.-L. (2018). The Reissner fiber in the cerebrospinal fluid controls morphogenesis of the body axis. Curr. Biol. *28*, 2479–2486.e4.
9. Zhang, X., Jia, S., Chen, Z., Chong, Y.L., Xie, H., Feng, D., Wu, X., Song, D.Z., Roy, S., and Zhao, C. (2018). Cilia-driven cerebrospinal fluid flow directs expression of urotensin neuropeptides to straighten the vertebrate body axis. Nat. Genet. *50*, 1666–1673.
10. Grimes, D.T., Boswell, C.W., Morante, N.F.C., Henkelman, R.M., Burdine, R.D., and Ciruna, B. (2016). Zebrafish models of idiopathic scoliosis link cerebrospinal fluid flow defects to spine curvature. Science *352*, 1341–1344.
11. Quan, F.B., Dubessy, C., Galant, S., Kenigfest, N.B., Djenoune, L., Leprince, J., Wyart, C., Lihrmann, I., and Tostivint, H. (2015). Comparative distribution and in vitro activities of the urotensin II-related peptides URP1 and URP2 in zebrafish: evidence for their colocalization in spinal cerebrospinal fluid-contacting neurons. PLoS ONE *10*, e0119290.
12. Agduhr, E. (1922). Über ein zentrales Sinnesorgan (?) bei den Vertebraten. Zeitschrift für Anatomie und Entwicklungsgeschichte *66*, 223–360.
13. Kolmer, W. (1921). Das "sagittalorgan" der wirbeltiere. Z. Anat. Entwicklungsgesch. *60*, 652–717.
14. Vigh, B., and Vigh-Teichmann, I. (1998). Actual problems of the cerebrospinal fluid-contacting neurons. Microsc. Res. Tech. *41*, 57–83.
15. Alfaro-Cervello, C., Soriano-Navarro, M., Mirzadeh, Z., Alvarez-Buylla, A., and Garcia-Verdugo, J.M. (2012). Biciliated ependymal cell proliferation contributes to spinal cord growth. J. Comp. Neurol. *520*, 3528–3552.
16. Böhm, U.L., Prendergast, A., Djenoune, L., Nunes Figueiredo, S., Gomez, J., Stokes, C., Kaiser, S., Suster, M., Kawakami, K., Charpentier, M., et al. (2016). CSF-contacting neurons regulate locomotion by relaying mechanical stimuli to spinal circuits. Nat. Commun. *7*, 10866.
17. Desban, L., Prendergast, A., Roussel, J., Rosello, M., Geny, D., Wyart, C., and Bardet, P.-L. (2019). Regulation of the apical extension morphogenesis tunes the mechanosensory response of microvilliated neurons. PLoS Biol. *17*, e3000235.
18. Djenoune, L., Desban, L., Gomez, J., Sternberg, J.R., Prendergast, A., Langui, D., Quan, F.B., Marnas, H., Auer, T.O., Rio, J.-P., et al. (2017). The dual developmental origin of spinal cerebrospinal fluid-contacting neurons gives rise to distinct functional subtypes. Sci. Rep. *7*, 719.
19. Djenoune, L., Khabou, H., Joubert, F., Quan, F.B., Nunes Figueiredo, S., Bodineau, L., Del Bene, F., Burcklé, C., Tostivint, H., and Wyart, C. (2014). Investigation of spinal cerebrospinal fluid-contacting neurons expressing PKD2L1: evidence for a conserved system from fish to primates. Front. Neuroanat. *8*, 26.
20. Orts-Del'Immagine, A., Kastner, A., Tillement, V., Tardivel, C., Trouslard, J., and Wanaverbecq, N. (2014). Morphology, distribution and phenotype of polycystin kidney disease 2-like 1-positive cerebrospinal fluid contacting neurons in the brainstem of adult mice. PLoS ONE *9*, e87748.
21. Huang, P., Xiong, F., Megason, S.G., and Schier, A.F. (2012). Attenuation of Notch and Hedgehog signaling is required for fate specification in the spinal cord. PLoS Genet. *8*, e1002762.
22. Park, H.-C., Shin, J., and Appel, B. (2004). Spatial and temporal regulation of ventral spinal cord precursor specification by Hedgehog signaling. Development *131*, 5959–5969.
23. Yang, L., Rastegar, S., and Strähle, U. (2010). Regulatory interactions specifying Kolmer-Agduhr interneurons. Development *137*, 2713–2722.
24. Petracca, Y.L., Sartoretti, M.M., Di Bella, D.J., Marin-Burgin, A., Carcagno, A.L., Schinder, A.F., and Lanuza, G.M. (2016). The late and dual origin of cerebrospinal fluid-contacting neurons in the mouse spinal cord. Development *143*, 880–891.
25. Hubbard, J.M., Böhm, U.L., Prendergast, A., Tseng, P.B., Newman, M., Stokes, C., and Wyart, C. (2016). Intraspinal sensory neurons provide powerful inhibition to motor circuits ensuring postural control during locomotion. Curr. Biol. *26*, 2841–2853.
26. Rodríguez, E.M., Rodríguez, S., and Hein, S. (1998). The subcommissural organ. Microsc. Res. Tech. *41*, 98–123.
27. Vigh, B., Vigh-Teichmann, I., and Aros, B. (1977). Special dendritic and axonal endings formed by the cerebrospinal fluid contacting neurons of the spinal cord. Cell Tissue Res. *183*, 541–552.
28. Vigh-Teichmann, I., and Vigh, B. (1983). The system of cerebrospinal fluid-contacting neurons. Arch. Histol. Jpn. *46*, 427–468.
29. Fidelin, K., Djenoune, L., Stokes, C., Prendergast, A., Gomez, J., Baradel, A., Del Bene, F., and Wyart, C. (2015). State-dependent modulation of locomotion by GABAergic spinal sensory neurons. Curr. Biol. *25*, 3035–3047.
30. Huang, A.L., Chen, X., Hoon, M.A., Chandrashekar, J., Guo, W., Tränkner, D., Ryba, N.J.P., and Zuker, C.S. (2006). The cells and logic for mammalian sour taste detection. Nature *442*, 934–938.
31. Wyart, C., Del Bene, F., Warp, E., Scott, E.K., Trauner, D., Baier, H., and Isacoff, E.Y. (2009). Optogenetic dissection of a behavioural module in the vertebrate spinal cord. Nature *461*, 407–410.
32. Jalalvand, E., Robertson, B., Tostivint, H., Wallén, P., and Grillner, S. (2016). The spinal cord has an intrinsic system for the control of pH. Curr. Biol. *26*, 1346–1351.
33. Jalalvand, E., Robertson, B., Wallén, P., and Grillner, S. (2016). Ciliated neurons lining the central canal sense both fluid movement and pH through ASIC3. Nat. Commun. *7*, 10002.
34. Orts-Del'Immagine, A., Seddik, R., Tell, F., Airault, C., Er-Raoui, G., Najimi, M., Trouslard, J., and Wanaverbecq, N. (2016). A single polycystic kidney disease 2-like 1 channel opening acts as a spike generator in cerebrospinal fluid-contacting neurons of adult mouse brainstem. Neuropharmacology *101*, 549–565.
35. Orts-Del'immagine, A., Wanaverbecq, N., Tardivel, C., Tillement, V., Dallaporta, M., and Trouslard, J. (2012). Properties of subependymal cerebrospinal fluid contacting neurones in the dorsal vagal complex of the mouse brainstem. J. Physiol. *590*, 3719–3741.
36. Sternberg, J.R., Prendergast, A.E., Brosse, L., Cantaut-Belarif, Y., Thouvenin, O., Orts-Del'Immagine, A., Castillo, L., Djenoune, L., Kurisu, S., McDearmid, J.R., et al. (2018). Pkd2l1 is required for mechanoception in cerebrospinal fluid-contacting neurons and maintenance of spine curvature. Nat. Commun. *9*, 3804.
37. Fernández-Llebrez, P., Pérez, J., Cifuentes, M., Alvial, G., and Rodríguez, E.M. (1987). Immunocytochemical and ultrastructural evidence for a neurophysinergic innervation of the subcommissural organ of the snake Natrix maura. Cell Tissue Res. *248*, 473–478.
38. Muñoz, R.I., Kähne, T., Herrera, H., Rodríguez, S., Guerra, M.M., Vío, K., Hennig, R., Rapp, E., and Rodríguez, E. (2019). The subcommissural organ and the Reissner fiber: old friends revisited. Cell Tissue Res. *375*, 507–529.
39. Reissner, E. (1860). Beiträge zur Kenntnis vom Bau des Rückenmarkes von Petromyzon fluviatilis L. Arch. Anat. Physiol. *77*, 545–588.
40. Brand, M., Heisenberg, C.P., Warga, R.M., Pelegri, F., Karlstrom, R.O., Beuchle, D., Picker, A., Jiang, Y.J., Furutani-Seiki, M., van Eeden, F.J.,

et al. (1996). Mutations affecting development of the midline and general body shape during zebrafish embryogenesis. Development *123*, 129–142.

41. Granato, M., and Nüsslein-Volhard, C. (1996). Fishing for genes controlling development. Curr. Opin. Genet. Dev. *6*, 461–468.
42. Jaffe, K.M., Grimes, D.T., Schottenfeld-Roames, J., Werner, M.E., Ku, T.-S.J., Kim, S.K., Pelliccia, J.L., Morante, N.F.C., Mitchell, B.J., and Burdine, R.D. (2016). c21orf59/kurly controls both cilia motility and polarization. Cell Rep. *14*, 1841–1849.
43. Thouvenin, O., Keiser, L., Cantaut-Belarif, Y., Carbo-Tano, M., Verweij, F., Jurisch-Yaksi, N., Bardet, P.-L., Van Niel, G., Gallaire, F., and Wyart, C. (2019). Origin of the bidirectionality of cerebrospinal fluid flow and impact on long-range transport between brain and spinal cord. bioRxiv. https://doi.org/10.1101/627166.
44. Becker, C.G., Becker, T., and Hugnot, J.-P. (2018). The spinal ependymal zone as a source of endogenous repair cells across vertebrates. Prog. Neurobiol. *170*, 67–80.
45. Becker, C.G., and Becker, T. (2015). Neuronal regeneration from ependymo-radial glial cells: cook, little pot, cook! Dev. Cell *32*, 516–527.
46. Jalalvand, E., Robertson, B., Wallén, P., Hill, R.H., and Grillner, S. (2014). Laterally projecting cerebrospinal fluid-contacting cells in the lamprey spinal cord are of two distinct types. J. Comp. Neurol. *522*, Spc1.
47. Troutwine, B., Gontarz, P., Minowa, R., Monstad-Rios, A., Konjikusic, M.J., Sepich, D.S., Kwon, R.Y., Solnica-Krezel, L., and Gray, R.S. (2019). The Reissner fiber is highly dynamic in vivo and controls morphogenesis of the spine. bioRxiv. https://doi.org/10.1101/847301.
48. Lauga, E., Brenner, M., and Stone, H. (2007). Microfluidics: the no-slip boundary condition. In Springer Handbook of Experimental Fluid Mechanics, C. Tropea, A.L. Yarin, and J.F. Foss, eds. (Springer Handbooks), pp. 1219–1240.
49. Olstad, E.W., Ringers, C., Hansen, J.N., Wens, A., Brandt, C., Wachten, D., Yaksi, E., and Jurisch-Yaksi, N. (2019). Ciliary beating compartmentalizes cerebrospinal fluid flow in the brain and regulates ventricular development. Curr. Biol. *29*, 229–241.e6.
50. Stoeckel, M.-E., Uhl-Bronner, S., Hugel, S., Veinante, P., Klein, M.-J., Mutterer, J., Freund-Mercier, M.-J., and Schlichter, R. (2003). Cerebrospinal fluid-contacting neurons in the rat spinal cord, a gamma-aminobutyric acidergic system expressing the P2X2 subunit of purinergic receptors, PSA-NCAM, and GAP-43 immunoreactivities: light and electron microscopic study. J. Comp. Neurol. *457*, 159–174.
51. Hudspeth, A.J. (2014). Integrating the active process of hair cells with cochlear function. Nat. Rev. Neurosci. *15*, 600–614.
52. Barral, J., and Martin, P. (2011). The physical basis of active mechanosensitivity by the hair-cell bundle. Curr. Opin. Otolaryngol. Head Neck Surg. *19*, 369–375.
53. Zur Lage, P., Newton, F.G., and Jarman, A.P. (2019). Survey of the ciliary motility machinery of *Drosophila* sperm and ciliated mechanosensory neurons reveals unexpected cell-type specific variations: a model for motile ciliopathies. Front. Genet. *10*, 24.
54. Karak, S., Jacobs, J.S., Kittelmann, M., Spalthoff, C., Katana, R., Sivan-Loukianova, E., Schon, M.A., Kernan, M.J., Eberl, D.F., and Göpfert, M.C. (2015). Diverse roles of axonemal dyneins in Drosophila auditory neuron function and mechanical amplification in hearing. Sci. Rep. *5*, 17085.
55. Didier, R., Dastugue, B., and Meiniel, A. (1995). The secretory material of the subcommissural organ of the chick embryo. Characterization of a specific polypeptide by two-dimensional electrophoresis. Int. J. Dev. Biol. *39*, 493–499.
56. Robles, E., Laurell, E., and Baier, H. (2014). The retinal projectome reveals brain-area-specific visual representations generated by ganglion cell diversity. Curr. Biol. *24*, 2085–2096.
57. Revenu, C., Streichan, S., Donà, E., Lecaudey, V., Hufnagel, L., and Gilmour, D. (2014). Quantitative cell polarity imaging defines leader-to-follower transitions during collective migration and the key role of microtubule-dependent adherens junction formation. Development *141*, 1282–1291.
58. Schindelin, J., Arganda-Carreras, I., Frise, E., Kaynig, V., Longair, M., Pietzsch, T., Preibisch, S., Rueden, C., Saalfeld, S., Schmid, B., et al. (2012). Fiji: an open-source platform for biological-image analysis. Nat. Methods *9*, 676–682.
59. Gobron, S., Monnerie, H., Meiniel, R., Creveaux, I., Lehmann, W., Lamalle, D., Dastugue, B., and Meiniel, A. (1996). SCO-spondin: a new member of the thrombospondin family secreted by the subcommissural organ is a candidate in the modulation of neuronal aggregation. J. Cell Sci. *109*, 1053–1061.
60. Schmid, B., Schindelin, J., Cardona, A., Longair, M., and Heisenberg, M. (2010). A high-level 3D visualization API for Java and ImageJ. BMC Bioinformatics *11*, 274.
61. López, M.G., Montiel, C., Herrero, C.J., García-Palomero, E., Mayorgas, I., Hernández-Guijo, J.M., Villarroya, M., Olivares, R., Gandía, L., McIntosh, J.M., et al. (1998). Unmasking the functions of the chromaffin cell alpha7 nicotinic receptor by using short pulses of acetylcholine and selective blockers. Proc. Natl. Acad. Sci. USA *95*, 14184–14189.
62. Reynolds, E.S. (1963). The use of lead citrate at high pH as an electron-opaque stain in electron microscopy. J. Cell Biol. *17*, 208–212.
63. R Development Core Team (2018). R: A language and environment for statistical computing (R Foundation for Statistical Computing). https://www.R-project.org/.

Please cite this article in press as: Orts-Del'Immagine et al., Sensory Neurons Contacting the Cerebrospinal Fluid Require the Reissner Fiber to Detect Spinal Curvature *In Vivo*, Current Biology (2019), https://doi.org/10.1016/j.cub.2019.12.071

STAR★METHODS

KEY RESOURCES TABLE

REAGENT or RESOURCE	SOURCE	IDENTIFIER
Antibodies		
Anti-Reissner fiber, Rabbit, polyclonal	[55]	
Anti-Pkd2l1, Rabbit, polyclonal	[36]	
Anti-tagRFP, Mouse, monoclonal (RF5R)	Thermo Fischer Scientific	Cat# MA5-15257, RRID:AB_10999796
Anti-GFP, Chicken	Abcam	Cat# ab13970 RRID:AB_300798
Anti-ZO-1	Invitrogen	Cat # 33-9100, RRID: AB_2533147
Alexa Fluor-568 goat anti-rabbit IgG	Molecular Probes	Cat# A11036, RRID:AB_10563566
Alexa Fluor-647 goat anti-rabbit IgG	Molecular Probes	Cat# A21244, RRID:AB_2535812
Alexa Fluor-555 goat anti-mouse IgG1	Molecular Probes	Cat# A21127 RRID:AB_2535769
Alexa Fluor-568 goat anti-mouse	Molecular Probes	Cat# A11004 RRID:AB_141371
Alexa Fluor-488 goat anti chicken IgG	Molecular Probes	Cat# A11039 RRID:AB_142924
Alexa Fluor-488 donkey anti rabbit IgG	Molecular Probes	Cat# A21206 RRID:AB_2535792
Chemicals, Peptides and Recombinant proteins		
A-Bungarotoxin	TOCRIS	Cat# 2133
Experimental Models: Organisms/Strains		
ZebraFish: *Tg(pkd2l1:GAL4)*^{icm10Tg}	[29]	ZFIN: ZBD-ALT-150324-1
ZebraFish: *Tg(pkd2l1:GCaMP5G)*^{icm07Tg}	[16]	ZFIN: ZDB-ALT-160119-4
ZebraFish: *Tg(UAS:TagRFP-CAAX;myl72:eGFP)*	[18]	ZFIN: ZDB-ALT-160119-7
ZebraFish: *Tg(UAS:mCherry)*	[56]	ZFIN: ZDB-ALT-130702-1
ZebraFish: *scospondin*^{icm15}	[8]	ZFIN: ZDB-ALT-181113-4
ZebraFish: *Tg(cdh2:cdh2-GFP, crybb1:ECFP)*	[57]	ZFIN: ZDB-ALT-141218-5
ZebraFish: *cfap298*^{tm304}	[40]	ZFIN: ZDB-ALT-980413-707
Software and Algorithms		
ImageJ	[58]	https://imagej.nih.gov/ij/
MATLAB	The MathWorks Inc.	http://www.mathworks.com/
Clampfit	Molecular Devices	N/A
R, version 3.5.2	The R project for statistical computing	http://cran.rptoject.org/
Huygens Professional, version 19.04	Scientific Volume Imaging, the Netherlands	http://svi.nl

LEAD CONTACT AND MATERIALS AVAILABILITY

Further information and requests for resources and reagents should be directed to and will be fulfilled by the Lead Contact, Claire Wyart (claire.wyart@icm-institute.org).

This study did not generate new unique reagents.

EXPERIMENTAL MODEL AND SUBJECT DETAILS

All procedures were performed on 3 days post fertilization (dpf) zebrafish larvae in accordance with the European Communities Council Directive (2010/63/EU) and French law (87/848) and approved by the Institut du Cerveau et de la Moelle épinière (ICM). All experiments were performed on *Danio rerio* embryos of AB, Tüpfel long fin (TL) and nacre background. Animals were raised at 28.5°C under a 14 / 10 light / dark cycle until the start of the experiment.

METHOD DETAILS

Immunohistochemistry

3 dpf larva were euthanized in 0.2% Tricaine (MS-222, Sigma-Aldrich, Saint Louis, Memphis, USA) in system water and fixed 2 hours in phosphate-buffered saline (PBS) containing 4% paraformaldehyde (PFA) and 3% sucrose at 4°C. After three washes in PBS, skin from the rostral trunk was partially removed and the yolk was removed. Samples were incubated overnight in a blocking buffer

containing 0.5% Triton, 1% DMSO, 10% normal goat serum (NGS) in PBS. Primary antibodies were incubated 48 hours at 4°C in a blocking buffer containing 0.5% Triton, 1% DMSO and 1% NGS. All secondary antibodies were from Molecular Probes© (Invitrogen, Life Technologies, Carlsbad, California, USA) unless specified and used at 1:500 in blocking buffer, and incubated 2.5 hours at room temperature. The following primary antibodies were used for *in toto* immunohistochemistry: rabbit anti-Reissner fiber (1:200, polyclonal, custom-made) [8, 59], rabbit anti-Pkd2l1 (1:200, custom-made) [36], mouse anti-tagRFP (1:500, MA515257, Thermo Fischer Scientific, Waltham, Massachusetts, USA), mouse anti-ZO-1 (1:200, 339100, Invitrogen) and chicken anti-GFP (1:500, ab13970, Abcam, Cambridge, England). The following secondary antibodies were used at 1:500: Alexa Fluor-568 goat anti-rabbit IgG A11036, Alexa Fluor-488 donkey anti-rabbit A21206, Alexa Fluor-647 goat anti-rabbit IgG A21244, Alexa Fluor-555 goat anti-mouse IgG1 A21127, Alexa Fluor-568 goat anti-mouse A11004, Alexa Fluor-488 goat anti chicken IgG A11039 (Thermo Fischer Scientific, Waltham, Massachusetts, USA).

Zebrafish larvae were mounted dorsally (for imaging in coronal plane) or laterally (for imaging in sagittal plane) in Vectashield® Antifade Mounting Medium (Vector Laboratories, Inc., Burlingame, California, USA) and imaged on an Olympus FV-1000 confocal microscope equipped with a 40X NA = 1.3 oil immersion objective (0.5 μm optical section and 0.35 μm optical section for images used to count contact with the RF (see Figure 5). Images were then processed using Fiji [58].

Analysis of the proximity between CSF-cNs and the RF

To image the Reissner fiber together with cerebrospinal fluid contacting neurons membranes in *Tg(pkd2l1:GAL4;UAS:tagRFP-CAAX)*, zebrafish larvae were mounted dorsally or laterally in Vectashield Antifade Mounting Medium (Vector Laboratories, Inc., Burlingame, California, USA) and imaged on an SP8 X White Light Laser Leica inverted confocal microscope equipped with a 63X oil immersion objective (NA = 1.4). Dorsally mounted larvae allowed acquiring coronal planes ideally oriented to access the apical extensions of dorsolateral cerebrospinal fluid contacting neurons, while laterally mounted larvae allowed acquiring sagittal planes ideally oriented to access the apical extensions of ventral cerebrospinal fluid contacting neurons (see Figure 5). Z stacks with a 250 nm step size (pixel size in the (x,y) plane: 144 nm) were acquired to estimate the proximity of the Reissner fiber with the apical extensions of cerebrospinal fluid contacting neurons in both cases. Four consecutive spinal cord regions were acquired along the rostro-caudal axis of the animals, respectively between segments 5 and 16. In order to correct for optical distortions taking place in the (x,y) and (z) planes, Z stacks were first deconvolved for both the Reissner fiber fluorescence signals and cerebrospinal fluid contacting neurons membrane signals, with the Huygens Professional version 19.04 (Scientific Volume Imaging, the Netherlands, http://svi.nl), using the CMLE algorithm, with a signal-to-noise ratio between 15 and 20, and up to 40 iterations. 3D stacks were then processed using Fiji [58]. Apposed or colocalized immunofluorescence signals from CSF-cNs and the Reissner fiber at least in a single plane after deconvolution were considered in close vicinity. The percentage of apical extensions in close vicinity with the Reissner fiber was then estimated for each fish. 3D views of the Reissner fiber and CSF-cNs from coronal and sagittal views (Figure 5E) were obtained using the 3D Viewer plugin on Fiji [60], after applying a median filter prior to 3D-segmentation.

Morphological Analysis

Analysis of the shape of the central canal

To measure the size of the central canal, we used 3 dpf zebrafish larvae where the apical junctions of the ependymal cells were visualized (with ZO-1 or Cadherin-2). For live imaging, we used the 3 dpf double transgenic *Tg(cdh2:cdh2-GFP; pkd2l1:GAL4;UAS:tagRFP-CAAX)* larva [57] in order to visualize the central canal and CSF-cNs *in vivo*. For images on fixed animals, we used antibodies against GFP (for cdh2-GFP), ZO-1 and tag-RFP. All images were acquired with an SP8 X White Light Laser Leica inverted confocal microscope equipped with a 40X water immersion objective (NA = 1).This image analysis was performed with Fiji. For the height of the canal, we acquired z stacks of sagittal confocal sections spaced by 1 μM. A max z-projection of the slices encompassing the canal (typically 5 to 10 slices) was performed, and the height of the fluorescent signal what measured at 4 different fixed levels (spaced by 30 μM) and averaged. For the width of the canal, we acquired z stacks of coronal confocal sections spaced by 1 μM. We observed frequently that the canal was not straight in this axis, preventing us from quantifying the width on z-projection. Instead, we quantified at 4 different fixed positions (spaced by 30 μM) the width of the fluorescent signal in the 5th slice above the floor plate signal (hence 4 μM above the floor plate), and averaged it.

Measurement of the size of CSF-cN apical extensions

To measure the size of the apical extension *in vivo*, we used 3 dpf *Tg(cdh2:cdh2-GFP; pkd2l1:GAL4;UAS:tagRFP-CAAX)* zebrafish larvae where CSF-cNs were visualized through RFP signal. All images were acquired with an SP8 X White Light Laser Leica inverted confocal microscope equipped with a 40X water immersion objective (NA = 1). To measure the height of the apical extension, we acquired z stacks of sagittal confocal sections spaced by 1 μM. A max z-projection of the slices encompassing each CSF-cNs was performed and we drew polygons outlining their apical extension using the polygon tool in Fiji.sc as described previously. An ellipse was fitted to the polygon and the height of the apical extension was measured as the height of the axis of the ellipse perpendicular to the floor plate as described previously [17, 18].

Calcium imaging

All experiments were done on 3 dpf *Tg(pkd2l1:GCaMP5G); scospondin*$^{icm15/icm15}$ and *Tg(pkd2l1:GCaMP5G); cfap298*$^{tm304/tm304}$ and their respective siblings used as controls (i.e., wild-type and heterozygous mutants from the same clutch).

Active muscle contraction

Unparalyzed 3 dpf larvae were pinned on their side through the notochord with 0.025cmm tungsten pins and bathed in artificial cerebrospinal fluid solution (aCSF, concentrations in mM: 134 NaCl, 2.9 KCl, 1.2 $MgCl_2$, 10 HEPES, 10 glucose and 2.1 $CaCl_2$; 290 mOsm.kg^{-1}, adjusted to pH 7.7–7.8 with NaOH). Active muscle contraction was induced by a 1 s-long pressure application of aCSF on the otic vesicle repeated 4-5 times with an inter trial interval of 1 minute. GCaMP5G fluorescence was excited by 490cnm illumination and monitored for 250 s at 4cHz using an Examiner epifluorescence microscope (Zeiss, Göttingen, Germany) equipped with a 40 X NA = 1.0 water-immersion objective and EMCCD camera ImagEM X2 (Hamamatsu, Naka-ku, Japan). Images were acquired using Labview software (National Instruments, Austin, Texas, USA) for *cfap298*^{tm304} mutants and using Hiris software (R&D Vision, Nogent-sur-Marne, France) for *scospondin*^{icm15} larvae and reconstructed using Fiji.

Passive spine bending

3 dpf larvae were anesthetized in 0.02% Tricain (MS-222, SIGMA dorsally mounted in glass-bottom dishes (MatTek, Ashland, Massachusetts, USA) filled with 1.5% low-melting point agarose. Larvae were paralyzed by injecting 0.5cnl of 0.5cmM α-Bungarotoxin in the musculature (Tocris Bioscience, Bristol, UK [61], and placed in aCSF. After embedding, roughly half of the larval tail was freed unilaterally to provide access to a blunt 50cμm diameter glass probe. Probe deflections were driven with a mechanotransducer device controlled through LabView software as done previously [16, 17]. Calcium imaging was performed on a two-photon laser scanning microscope (2p-*vivo*, Intelligent Imaging Innovations, Inc., Denver, USA) using a 20X NA = 1.0 objective. Lateral bending of the tail was induced by probe deflection and repeated 3 times every 14 to 17.5 s as done previously [16, 17].

Calcium imaging analysis

Slow translational drifts of the image due to spine movement were corrected using image registration by taking as a reference image a max Z-projection of 3 consecutive images chosen when CSF-cNs are back to their position and bright after a muscle contraction. The regions of interest (ROI) corresponding to each individual cell were drawn manually on the reference image. We identified CSF-cN calcium transients in response to spinal curvature by using either the motion artifact itself or a 200 ms-long flash of green light performed 16 s before the stimulus. The amplitude of the first CSF-cN calcium transients in response to passive and active spinal concave curvature were determined relative to baseline preceding the motion artifact with custom scripts written in MATLAB (MathWorks, Natick, Massachusetts, USA). For each contraction and each ROI, ΔF / F was estimated as (F_{GCaMP} - $F_{0\text{-}GCaMP}$) / $F_{0\text{-}GCaMP}$ with F_{GCaMP} is the fluorescence signal averaged over four time points (i.e., 1 s) around the peak after the first contraction and $F_{0\text{-}GCaMP}$ is the baseline fluorescence average over 3 time points (i.e., 0.75 s) before each motion artifact. For each contraction, a new baseline was therefore estimated to prevent errors due to photobleaching or drifting during the recording. The percentage of responding cell was set as ΔF / F > 1.96 STD of the minimum value during the motion artifact.

In vivo patch-clamp recording

Whole-cell recordings were performed in aCSF on 3 dpf *Tg(pkd2l1:Gal4; UAS:mCherry)* carrying either the *scospondin*^{icm15} or *cfap298*^{tm304} mutation and their respective control siblings. Larva were pinned through the notochord with 0.025mm diameter tungsten pins. Skin and muscle from two to three segments around segment 10 were dissected out using a glass suction pipette. A MultiClamp 700B amplifier, a Digidata series 1440 A Digitizer, and pClamp 10.3 software (Axon Instruments, Molecular Devices, San Jose, California, USA) were used for acquisition. Raw signals were acquired at 50 kHz and low-pass filtered at 10 kHz. Patch pipettes (1B150F-4, WPI) with a tip resistance of 5–8MΩ were filled with internal solution (concentrations in mM: K-gluconate 115, KCl 15, MgCl2 2, Mg-ATP 4, HEPES-free acid 10, EGTA 5 or 10, 290 mOsm/L, pH adjusted to 7.2 with KOH with Alexa 488 at 40 μM final concentration). Holding potential was −85 mV, away from the calculated chloride reversal potential (E_{Cl} = − 51 mV). Analysis of electrophysiological data was performed offline using Clampex 10 software (Molecular Devices, San Jose, California, USA). Single channel events were identified using single-channel search in Clampfit (Molecular Devices, San Jose, California, USA), with a first level set at −15 pA from the baseline (level 0). Only events lasting longer than 1.2 ms were included for analysis. A 20 s window was used to identify channel events from a gap-free voltage-clamp recording from the first 1 to 3 min of recording. Passive properties were determined, in voltage-clamp mode at −85 mV, from the cell current response to a 10 mV hyperpolarization step (V step). Membrane resistance (R_m) was estimated from the amplitude of the sustained current at the end of the 100 ms voltage step (R_m = V step / Im). Membrane capacitance (C_m) was estimated as the ratio between the cell decay time constant (t), obtained from the exponential fit of the current decay an R_S (C_m ∼t / R_S). Action potential discharge was monitored in current-clamp mode in response to successive depolarizing current steps of 100 ms from – 2 pA to + 28 pA steps with a 2 pA increment after a fixed prepulse with −10 pA for 20 ms while holding the cell membrane potential at - 50 mV.

Electron microscopy

All the products used for electron microscopy were obtained from Electron Microscopy Science (EMS, distributor Euromedex, Soufleweyesheim, France).

Transmission electron microscopy

Samples were fixed in 0.5% glutaraldehyde 4% PFA in PBS, pH 7.4 for 2 hours at 4°C. Some samples were treated with 1% trichloroacetic acid (TCA) within the fixative solution in order to better visualize preserve the Reissner fiber (as shown in Figures 6A1–6A3). Following three rinses with Na-cacodylate buffer 0.1 M pH = 7.4, sections were post-fixed with 1% osmium tetroxide in the same buffer for 1 hour. Samples were dehydrated in a graded series of ethanol solutions (75, 80, 90 and 100%, 5min each). Final dehydration was performed twice in 100% acetone for 20 min. Infiltration with epoxy resin (Epon 812) was performed in 2 steps: overnight at + 4°C in a 1:1 mixture of resin and acetone in an airtight container and then, 2 hours at room temperature (RT) in pure resin. Finally, samples were placed in molds with fresh resin and cured at 56°C for 48 hours in a dry oven. Samples were sagittally cut in 0.5 μm semi-thin sections with an ultramicrotome EM UC7 (Leica, Wetzlar, Germany). Sections were stained with 1% toluidine in borax buffer 0.1 M. Then ultra-thin sections (~70nm thick) were cut and collected on copper grid. Sections were then contrasted with Reynolds lead citrate for 7min [62]. Observations were made with a HT 7700 electron microscope operating at 70kV (Hitachi, Ltd, Tokyo, Japan). Electron micrographs were taken with an integrated AMT XR41-B camera (2048 × 2048 pixels, Advanced Microscopy Techniques Corp., Woburn, Massachusetts, USA).

Serial block face scanning electron microscopy

Samples (as shown in Figure 6C and Video S3) were fixed in 0.5% glutaraldehyde 4% PFA in PBS pH 7.4 for 2 hours at 4°C. Following three rinses with Na-cacodylate buffer 0.1M pH = 7.4, sections were post-fixed for 30 minutes with 0.1% tannic acid in caco buffer as a mordant. After three rinses in caco buffer, samples were stained in freshly prepared (1% OsO_4; 0,15% $K_4Fe(CN)_6$) solution for 1 hour. Samples underwent multiple incubation steps to increase the contrast: 20 min in 0.01% thiocarbohydrazide (TCH) at 60°C, 30 minutes in 1% OsO_4, 60 min at 4°C in 1% aqueous uranyl acetate and 30 min in a 0.66% lead nitrate in 30 mM aspartic acid solution, pH = 5.5 at 60°C. Samples were dehydrated in graded ethanol at room temperature with a final dehydration in 100% acetone. Samples were then embedded in 50% resin / 50% acetone overnight at +4°C and dry at 60°C for 48 hours. Samples were sagittally sectioned in 7 nm-thick sections every 40 nm and imaged with a SBF-SEM. Sectioning and scanning were performed with a TeneoVS electron microscope (FEI Company, Hillsboro, Oregon, USA) operating at 2kV-100pA- low vacuum (40Pa)-dwell time 1μs. Subsequently, 3D reconstruction was made using the Imaris software (Oxford instruments, Zurich, Switzerland).

QUANTIFICATION AND STATISTICAL ANALYSIS

All values are mean ± standard error of the mean (SEM) and represented as a boxplot where the central mark on indicates the median, the bottom and top edges of the box indicate the 25th and 75th percentiles. The whiskers extend to the most extreme data points that are not considered outliers, outliers are identified with a "+" symbol.

Patch-clamp recording and Morphological study

Statistical significance was determined using Two-sample Kolmogorov-Smirnov test (kstest2, MATLAB, MathWorks, Natick, Massachusetts, USA). A value of $p \leq 0.05$ was considered significant.

Calcium imaging

Stimulus artifact have been digitally removed in all figures. The data were analyzed with the repeated-measure design. Values obtained from the response to active stimulation were analyzed using linear mixed-effects models (LMMs) with condition (control versus mutant) and domain (dorsolateral versus ventral CSF-cNs) as fixed effects and each independent fish (nested within clutch) as a random effect to account for the repeated-measurements. Significance for the main effects of condition, domain and their interaction were then evaluated using ANOVA Type II Wald chi-square tests. The same analysis was conducted with the values obtained from response to passive stimulation, but for the condition factor only. All statistical analyses were conducted using R version 3.5.2 [63] and plots were generated with the ggplot2 package. All LMMs were fitted using the function lmer in the lme4 package. ANOVA Type II Wald chi-square tests were performed using the function anova in the car package. Post hoc Tukey's comparisons of the conditions within domains were made and plotted using the estimated marginal means from the emmeans package. To improve normality and homoscedasticity of residuals in the LMMs, response data were square root transformed on absolute values and then returned to their original sign prior to analysis. The level of statistical significance was set at $p < 0.05$ for all tests (see Methods S1).

DATA AND CODE AVAILABILITY

The codes generated during this study are available at Github. https://github.com/wyartlab/Orts-Del-Immagine_CurrentBio_2020

The published article includes all statistical datasets generated during this study (see Methods S1).

Current Biology, Volume *30*

Supplemental Information

Sensory Neurons Contacting the Cerebrospinal Fluid Require the Reissner Fiber to Detect Spinal Curvature *In Vivo*

Adeline Orts-Del'Immagine, Yasmine Cantaut-Belarif, Olivier Thouvenin, Julian Roussel, Asha Baskaran, Dominique Langui, Fanny Koëth, Paul Bivas, François-Xavier Lejeune, Pierre-Luc Bardet, and Claire Wyart

	Active stimulation				**Passive stimulation**	
	Control sibling		***cfap298***$^{tm304/tm304}$		**Control sibling**	***cfap298***$^{tm304/tm304}$
	Dorsolateral	Ventral	Dorsolateral	Ventral	Dorsolateral	Dorsolateral
Mean dF/F, %	87.2	57.4	19.0	15.5	100.7	32.3
SEM	5.0	3.3	1.9	1.4	4.3	2.7
n, cells	211	168	153	104	830	490
N, fish	15	15	11	11	26	15
Response, %	68.2	64.3	29.4	31.7	62.2	28.4
p, Dl vs. Ventral in control sibling	**<0.0001**					
Df	**613**					
p, Dl vs. Ventral in cfap298	**0.529**					
Df	**614**					
p, control vs. *cfap298* in Dl CSF-cNs	**<0.0001**				**1.6 x 10**$^{-9}$	
Df	**30.4**				**1**	
p, control vs. *cfap298* in ventral CSF-cNs	**0.007**					
Df	**32.9**					

Table S1. Response of CSF-cNs to spine curvature in control sibling and in *cfap298*$^{tm304/tm304}$. Related to Figure 1. Dl: dorsolateral CSF-cNs.

	NP$_0$		I$_{channel}$, pA		Single event duration, ms	
Recorded cell	**Control sibling**	***cfap298***$^{tm304/tm304}$	**Control sibling**	***cfap298***$^{tm304/tm304}$	**Control sibling**	***cfap298***$^{tm304/tm304}$
1	0.0005	0.0006	-17.4	-13.8	2.4	4.2
2	0.0012	0.0003	-18.5	-19.5	3.3	2.5
3	0.0004	0.0042	-19.8	-17.2	2.3	2.9
4	0.0004	0.0003	-18.4	-19.0	3.3	2.6
5	0.0025	0.0003	-19.2	-20.7	2.4	2.2
6	0.0005	0.0004	-19.4	-19.5	1.8	2.5
7	0.0010		-19.9		2.9	
8	0.0003		-17.2		6.5	
9	0.0009		-19		2.7	
Mean	**0.0009**	**0.0010**	**-18.8**	**-18.3**	**3.0**	**2.8**
SEM	**0.0002**	**0.0006**	**0.3**	**1.0**	**0.5**	**0.3**
N, cells	**9**	**6**	**9**	**6**	**9**	**6**
p	**0.53**		**0.89**		**0.89**	
Ks2stat	**0.39**		**0.28**		**0.28**	

Table S2. Single channel opening properties of CSF-cNs measured in control and *cfap298*$^{tm304/tm304}$. Related to Figure 2B and 2C. NP$_0$: channel opening probability, I$_{channel}$: single channel current amplitude.

	r_m, GΩ		**c_m, pF**		**V_r, mV**	
Recorded cell	**Control sibling**	***cfap298*$^{tm304/tm304}$**	**Control sibling**	***cfap298*$^{tm304/tm304}$**	**Control sibling**	***cfap298*$^{tm304/tm304}$**
1	8.4	1.7	2.1	2.0	-49.0	-40
2	2.7	3.3	2.2	2.1	-41	-48
3	3.7	5.1	2.2	2.1	-47	-44
4	2.8	3.3	3.0	1.8	-41	-43
5	2.8	2.4	1.5	2.5	-44	-45
6	1.9	9.8	2.6	2.4	-40	
7	2.2	12.8	2.4	1.7	-43	
8	4.0		2.0		-42	
9	6.0		2.2			
10	3.2		1.7			
11	5.3		2.2			
Mean	**3.9**	**5.5**	**2.2**	**2.1**	**-43.4**	**-44**
SEM	**0.6**	**1.6**	**0.1**	**0.1**	**1.1**	**1.3**
N, cells	**11**	**7**	**11**	**7**	**8**	**5**
p	0.807		0.28		0.89	
Ks2stat	0.29		0.44		0.30	

Table S3. Intrinsic properties of CSF-cNs measured in control and *cfap298*$^{tm304/tm304}$. Related to Figure 2D. r_m: membrane resistance, c_m: membrane capacitance, V_r: resting potential

	Active stimulation				**Passive stimulation**	
	Control sibling		***scospondin*$^{icm15/icm15}$**		**Control sibling**	***scospondin*$^{icm15/icm15}$**
	Dorsolateral	Ventral	Dorsolateral	Ventral	Dorsolateral	Dorsolateral
Mean dF/F, %	57.3	31.3	7.1	10.9	194.0	56.2
SEM	3.0	2.1	0.6	1.4	17.8	13.1
n, cells	180	128	167	146	276	165
N, fish	12	12	11	11	11	8
Response, %	65.0	58.6	6.0	13.0	60.9	17.0
p, Dl vs. Ventral in control sibling	**<0.0001**					
Df	**602**					
p, Dl vs. Ventral in *scospondin*$^{icm15/icm15}$	**0.08**					
Df	**601**					
p, control vs. *scospondin*$^{icm15/icm15}$ in Dl CSF-cNs	**<0.0001**				**0.00424**	
Df	**21.4**				**1**	
p, control vs. *scospondin*$^{icm15/icm15}$ in ventral CSF-cNs	**0.0004**					
Df	**22.6**					

Table S4. Response of CSF-cNs to spine curvature in control sibling and in *scospondin*$^{icm15/icm15}$. Related to Figure 3. Dl: dorsolateral CSF-cNs.

	NP_0		$I_{channel}$, pA		Single event duration, ms	
Recorded cell	**Control sibling**	***scospondin*$^{icm15/icm15}$**	**Control sibling**	***scospondin*$^{icm15/icm15}$**	**Control sibling**	***scospondin*$^{icm15/icm15}$**
1	0.0006	0.0016	-17.4	-17.0	4.7	2.3
2	0.0012	0.0011	-18.5	-18.9	3.8	4.0
3	0.0075	0.0002	-19.4	-15.2	2.9	5.4
4	0.0019	0.0011	-18.7	-19.8	5.0	2.5
5	0.0010	0.0019		-19.3	2.3	12.3
6		0.0036		-21.9		4.3
Mean	**0.0024**	**0.0016**	**-18.6**	**-18.7**	**3.7**	**5.1**
SEM	**0.0013**	**0.0005**	**0.3**	**0.9**	**0.5**	**1.5**
N, cells	**5**	**6**	**5**	**6**	**5**	**6**
p	**0.99**		**0.85**		**0.85**	
Ks2stat	**0.23**		**0.33**		**0.33**	

Table S5. Single channel opening properties of CSF-cNs measured in control and *scospondin*$^{icm15/icm15}$. Related to Figure 4B and 4C. NP_0: channel opening probability, $I_{channel}$: single channel current amplitude.

	r_m, GΩ		**c_m, pF**		**V_r, mV**	
Recorded cell	**Control sibling**	***scospondin*$^{icm15/icm15}$**	**Control sibling**	***scospondin*$^{icm15/icm15}$**	**Control sibling**	***scospondin*$^{icm15/icm15}$**
1	5.3	7.2	2.3	3.1	-40	-44
2	5.3	3.9	3.0	1.3	-48	-49
3	6.4	18.5	1.9	2.1	-45	-45
4	4.8	10.3	2.2	2.0	-49	-40
5	6.1	8.8	2.0	2.0		
6	13.6	13.7	1.6	2.0		
Mean	**6.9**	**10.4**	**2.2**	**2.1**	**-45.5**	**-44.5**
SEM	**1.4**	**2.1**	**0.2**	**0.2**	**2.0**	**1.8**
N, cells	**6**	**6**	**6**	**6**	**4**	**4**
p	0.08		0.81		1.00	
Ks2stat	0.67		0.33		0.25	

Table S6. Intrinsic properties of CSF-cNs measured in control and *scospondin*$^{icm15/icm15}$. Related to Figure 4D. r_m: membrane resistance, c_m: membrane capacitance, V_r: resting potential

	Height of the central canal		**Width of the central canal**		**Height of the apical extension**		**Width of the apical extension**	
	Cadherin-GFP *in vivo*	**ZO-1 staining in fixed tissue**	**Cadherin-GFP *in vivo***	**ZO-1 staining in fixed tissue**	***in vivo***	**Fixed tissue**	***in vivo***	**Fixed tissue**
Mean diameter, µm	10.2	14.1	8.7	3.5	2.9	3.6	5.2	4.4
SEM	0.7	1.2	0.4	0.3	0.1	0.2	0.3	0.3
n, cells					9	12	9	12
N, fish	9	13	4	10	4	4	4	4
p	0.02		0.0018		0.103		0.051	
Ks2stat	0.62		1		0.500		0.556	

Table S7. Comparison of the size of the central canal and the CSF-cN apical extension in live and fixed tissue. Related to Figure 5.